

JOINT INSTITUTE FOR NUCLEAR RESEARCH

Laboratory of Radiation Biology

**FINAL REPORT ON THE
START PROGRAMME**

Treatment planning and dosimetry at the SARRP facility

Supervisor:

Ivan Sergeevich Gordeev

Student:

Anthony Walwyn Cadenas, Cuba

University of Havana

Participation period:

July 28 – September 21,

Summer Session 2024

Dubna, 2024

Contents

Abstract	4
Introduction	5
1 Literature overview	7
1.1 The production and properties of X-Rays	7
1.1.1 The basic X-Ray tube scheme	7
1.2 X-Rays spectra	9
1.2.1 Bremsstrahlung	12
1.2.2 Characteristic radiation	12
1.3 The basic interactions of photons with matter	15
1.3.1 Attenuation coefficients	17
1.3.2 Photoelectric effect	21
1.3.3 Rayleigh scattering	22
1.3.4 Compton scattering	22
1.4 Basic dosimetry and beam-quality characterization	24
1.4.1 Field and dosimetry quantities	24
1.4.2 Percentage Depth Dose	26
1.4.3 Beam quality characteristics	27
2 Materials and methods	30
2.1 General information and capabilities of SARRP facility	30
2.2 Mouse phantom manufacturing	33
2.3 Film dosimetry	35
2.3.1 Gafchromic EBT3 films	36
2.3.2 Preparation of Gafchromic EBT3 films for irradiation	37
2.3.3 Gafchromic EBT3 films calibration process	41
2.4 Monte Carlo calculations for experiment verification	43
2.4.1 FLUKA software description	45

2.4.2	Modeling of experiment with mouse phantom in FLUKA .	46
2.5	Experiment and modeling workflow	48
3	Results and discussion	54
	Conclusion	62
	References	64

Abstract

During the internship, the literature on the production and properties of X-Rays as well as main dosimetry principles were studied. It was possible to get acquainted with X-ray machines designed for irradiation of various biological objects which are at routine use at the LRB JINR. The main tasks were to learn how to work with the radiation therapy planning system (TPS) MuriPlan on the SARRP facility and to create a simplified mouse phantom for further dosimetric work with various X-ray beam qualities of SARRP machine.

Introduction

The Small Animal Radiation Research Platform (SARRP) facility is a cutting-edge system used in preclinical studies for precise image-guided radiotherapy in small animal models. The SARRP combines X-ray imaging with highly accurate radiation delivery, making it a key tool in cancer research and radiobiology. Central to its operation is treatment planning, which allows for the careful calculation of radiation doses to ensure effective tumor targeting while minimizing exposure to surrounding healthy tissues. The MuriPlan software is integral to this process, enabling the creation of detailed treatment plans through Cone Beam Computed Tomography (CBCT) imaging and dose calculation algorithms.

In radiotherapy research, phantoms are indispensable for validating treatment plans and dosimetry measurements. These models simulate the physical and radiological properties of biological tissues, allowing researchers to test and calibrate treatment protocols before applying them to live subjects. Specifically, the use of film dosimetry is a well-established technique in this context. Radiochromic films like Gafchromic EBT3 offer high spatial resolution and energy independence, making them an ideal choice for measuring absorbed doses and verifying treatment accuracy.

Monte Carlo simulations further enhance the precision of these experiments. Tools such as FLUKA are commonly employed to simulate radiation transport and interactions within the phantom, providing valuable insights that complement experimental data. These simulations help predict dose distributions and assess the overall accuracy of the dosimetry process, reducing uncertainties and improving the quality of preclinical research.

This study was conducted at the Laboratory of Radiation Biology (LRB) within the Joint Institute for Nuclear Research (JINR), a leading center for advanced radiation research. Particularly, at the LRB the SARRP machine is applied

to conduct studies in the field of radioprotective and radiosensitizing agents using small animals. The motivation behind this project stems from the need to refine dosimetry techniques and treatment planning protocols in small animal models, thereby contributing to the development of more effective radiotherapy treatments. Understanding the intricacies of treatment planning, phantom calibration, and dosimetry is essential for improving radiation-based therapies and advancing preclinical studies in radiobiology.

1 Literature overview

In the present section a review of the main aspects from bibliography is done. A basic explanation of everything in our interest is made, starting from the production of X-rays and the interaction of them with matter.

1.1 The production and properties of X-Rays

Nowadays X-ray tubes are not designed as they were in 1895, when they were discovered by Wilhelm Roentgen. The latter used a so-called Crookes tube, which was nothing more than a partially evacuated gas tube, two electrodes inside it and a voltage source to cause a potential difference to ionize the atoms of the gas contained in the tube. After this ionization cascade the free electrons were accelerated by the potential difference and hit both the tube walls and the anode. The deceleration of the colliding electrons produce, by various mechanisms, the so-called X-rays [1].

1.1.1 The basic X-Ray tube scheme

In contrast to the previously described tubes, known as cold tubes (which name makes sense when compared to the way of generating X-rays that is currently used), others are currently used which have a completely different principle of electron generation, thermionic emission. Figure 1 shows a simplified schematic of a modern X-ray production equipment.

In this case the high voltage source (U), like in the previous case, is used to create a potential difference between the cathode (C) and anode (A) which are in a vacuum tube (V). Electron emission in this case is achieved by using the thermionic effect, which is the process of releasing electrons from a hot tungsten filament when current flows through it. This current controls the charge reaching the target

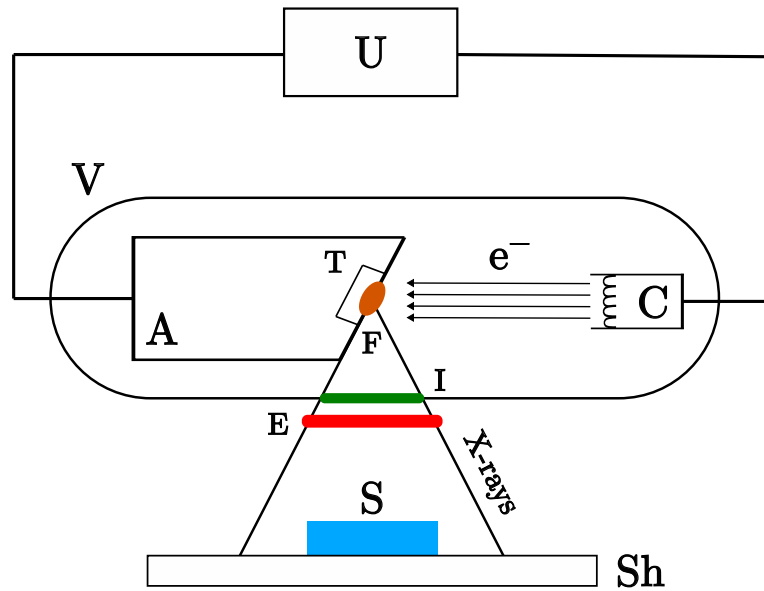


Figure 1: Simplified scheme of a typical X-ray tube setting. U — High voltage source, V — Vacuum tube, A — Anode, C — Cathode, T — Target, F — Focal spot, e^- — electrons, I — Inherent filtration, E — External (added) filtration, S — Sample, Sh — Shelf.

per unit of time. The number of electrons striking the target N , is proportional to the current i and the time T of current applied:

$$N \propto iT \quad (1)$$

For the kilovoltages range, which is the range that we work on (specifically 225 kV in the SARRP facility), less than 1 % of the energy carried by the electrons is converted in X-rays and approximately the 99 % is turned into heat. The total energy, deposited in the anode target is proportional to the voltage U and current i applied:

$$W \propto iU \quad (2)$$

The heat needs to be removed from the anode for the correct functioning of the machine, that is why one part of the anode is made of a material to better dissipate heat (usually copper). The other part is known as the target (T) made of heavy elements such as tungsten, rhenium, rhodium, molybdenum, or an alloy. The place where the electrons are focused on, is called focal spot (F). When the electrons interact

with the target, by different mechanisms, the X-rays are emitted. The amount of energy carried by the electrons, that is converted into X-rays, is called efficiency of the X-rays ϵ . The efficiency is proportional to the atomic number Z of target material and voltage applied:

$$\epsilon \propto ZU \quad (3)$$

That's the reason why the target material of the anode is usually made of heavy elements [1].

At least one half of the X-rays are absorbed in the target itself, of the remaining portion only those that emerge in the cone of the primary beam [2]. This absorption in the target is called inherent filtration, this kind of filtration also includes components like the exit window (I) and housing of the X-ray tube. There is also another type of filtration called external (added) filtration, as its name suggest, this filtration occurs when we place external filters (E) on the exit of the X-rays. In general filtration reduces X-ray intensity of the whole energy range, but the most effective filtering is on the low energy range of X-rays. The change in the shape of the beam spectrum with filtration is referred to as beam hardening. This low energy X-rays would cause a greater biological effect on the sample, that's why we usually use added filtration. The average X-ray energy is increased and becomes more penetrating. Depending on the application, beryllium, aluminum, copper or tin are commonly used for filtration [3]. After the filtration the X-rays finally get to the sample (S) place on the shelf (Sh), to fulfill its function.

1.2 X-Rays spectra

The effects on the sample after irradiation will be different depending on the spectrum of the X-ray beam. The spectrum of a beam of electromagnetic radiation helps to understand the different processes involved in its generation. To better understand X-rays, we must analyze a typical X-ray beam spectra. Figure 2

illustrates an example of these spectra.

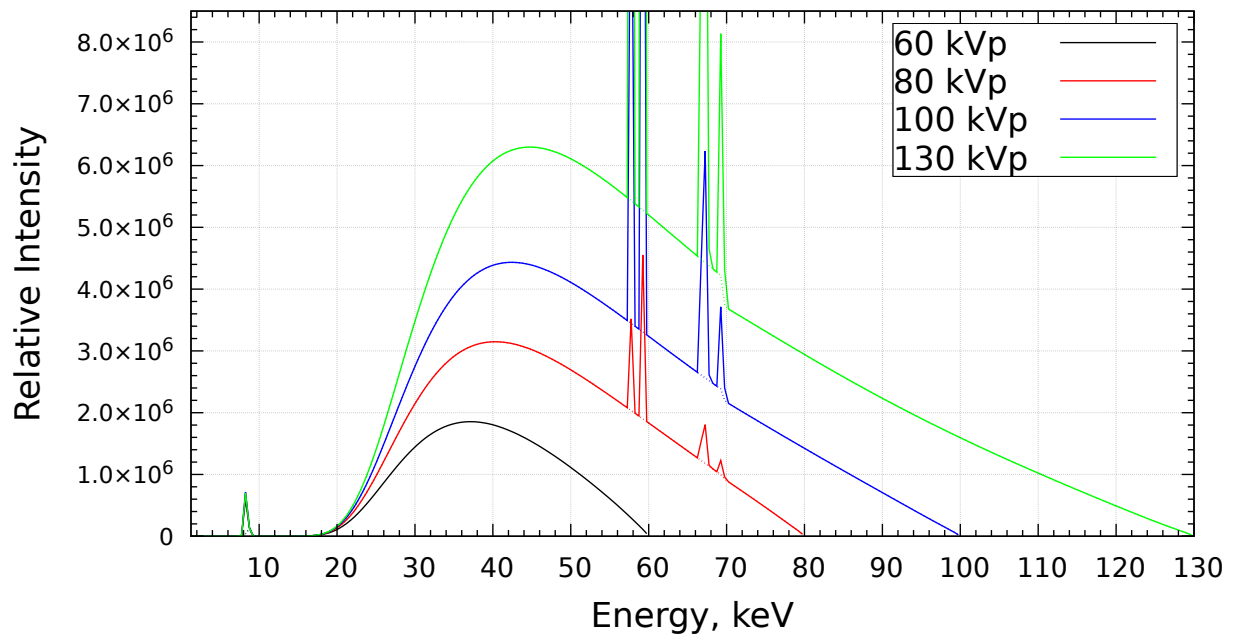


Figure 2: Typical X-ray beam spectra (at different voltage)

In this figure on the x-axis we have the energy of photons in keV, and on the y-axis the relative intensity for each of these energies. In the graph one can clearly distinguish a continuous part, corresponding to the braking radiation or bremsstrahlung. The other part, composed of discrete peaks, is the so-called characteristic radiation. To illustrate the possible mechanisms of electron interaction with the target we use Figure 3 [2, p. 61].

Track “a” shows different collisions where the direction of the incident electron is changed several times, its energy is given up to the atoms of the material, triggering ionization processes. In general most of the electron energy will be converted into heat, as it was mentioned earlier. Among the electrons that are taken out of the atoms, there are a few that have enough energy to produce additional ionizations, the so-called delta rays. The remaining processes are much rarer than this.

In track “b” the electron’s energy is enough to take out the electrons from the K shell of the atom. Then, an electron from higher shells takes its place, this

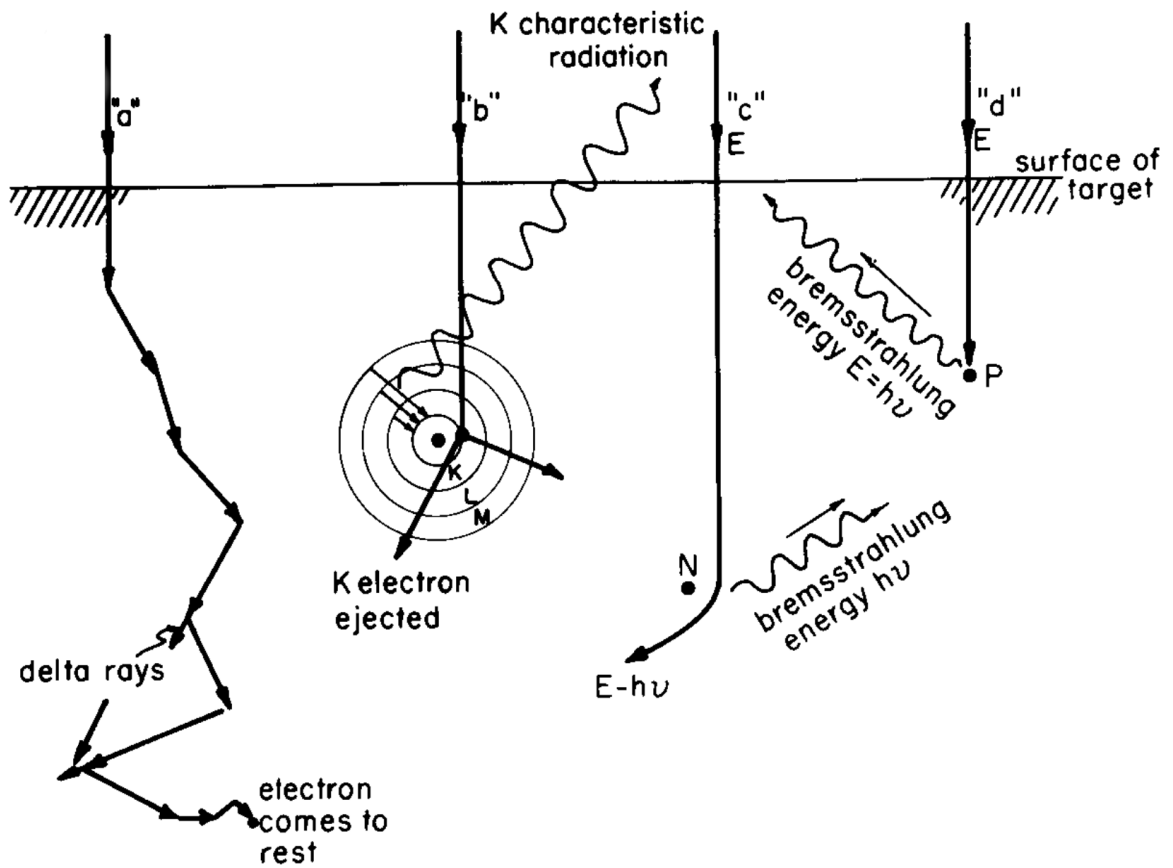


Figure 3: Typical electron interactions with a target [2, p. 61]

transition is accompanied by an emission of a photon that will have energy equal to the difference between the two levels involved in the transition, in the illustrated case it will be a characteristic K radiation. If the electron does not have enough energy to knock out one of the K shell this process will not occur.

In track “c” occasionally the electron will pass very close to the nucleus (N) of the atom, due to the interaction between the positive charges of the nucleus and the negative charge of the electron, the latter is made to orbit partially around the nucleus. The electron will recede from this interaction with its energy reduced. This loss of energy will give rise to a photon with energy $h\nu$ and the primary electron will recoil with energy $E - h\nu$. This sudden deceleration gives rise to bremsstrahlung or “break radiation”.

Track “d” represents an improbable interaction when an electron is suddenly stopped in a collision, all its energy appears as bremsstrahlung.

All the processes described above are complex and can all occur in one track. For example, an electron could undergo many ionization losses, then a radiation loss, more ionization losses and finally come to rest. Moreover, they could occur at any depth in the target. The radiation that is produced must emerge before it is useful, so radiation that occurs near the edge of the material is more likely to emerge than others [2].

1.2.1 Bremsstrahlung

In the previous section it was explained that if an electron comes close to an atomic nucleus (Figure 3, track “c”), the attractive Coulomb forces cause a change of the electron’s trajectory. An accelerated electron, or an electron changing its direction, emits electromagnetic radiation and this energy of the emitted photon is subtracted from the kinetic energy of the electron. The energy of the bremsstrahlung photon depends on the attractive Coulomb forces and hence on the distance of the electron from the nucleus. So, this process is responsible for the continuous part of the X-ray spectra [4].

1.2.2 Characteristic radiation

Another process which takes an important part in the X-ray spectrum is when a fast electron colliding with an electron of an atomic shell could knock out the electron (Figure 3, track “b”). The process occurs if the kinetic energy of the electron exceeds the binding energy of the electron in that shell. The scattered primary electron carries away the difference of kinetic energy and binding energy. The vacancy in the shell is then filled with an electron from an outer shell, accompanied by the emission of an X-ray photon with an energy equal to the difference in binding energies of the shells involved. For each element, binding energies, and the monoenergetic radiation resulting from such interactions, are unique and charac-

teristic for that element. For example, K radiation denotes characteristic radiation for electron transitions to the K shell, and likewise, L radiation for transitions to the L shell. The origin of the electron filling the vacancy is indicated by suffixes α, β, γ , etc where α stands for a transition from the adjacent outer shell, β from the next outer shell, etc. K_α radiation results from L to K shell transitions; K_β radiation from M to K shell transitions, etc. Energies are further split owing to the energy levels in a shell, indicated with a numerical suffix. Further, each vacancy in an outer shell following from such a transition gives rise to the emission of corresponding characteristic radiation causing a cascade of photons [4].

Table 1 shows information of several lines from different elements, usually used for target materials in anodes of X-ray tubes. In each row there is a characteristic line for every element and in each cell the top line is energy (in keV) and the bottom line is intensity, the strongest have 100. That's why we expect to see, along the continuous part of the X-ray spectra, a set of discrete peaks, depending on the material of the X-ray tube used.

Table 1: Characteristic photon energies and relative intensities for the set of elements, used as targets in X-ray tubes. In each cell the top line is energy (in keV) and the bottom line is intensity, the strongest have 100 [5, p. 1-15 – 1-27]

	Mo, Z = 42	Rh, Z = 45	W, Z = 74	Re, Z = 75
K_{α_1}	17.479	20.216	59.318	61.140
	100	100	100	100
K_{α_2}	17.374	20.074	57.982	59.718
	52	53	58	58
K_{β_1}	19.608	22.724	67.244	69.310
	15	16	22	22
K_{β_2}	19.590	23.173	69.067	71.232
	3	4	8	8

Table 1 continued from previous page

	Mo, Z = 42	Rh, Z = 45	W, Z = 74	Re, Z = 75
K_{β_3}	19.965	22.698	66.9514	68.994
	8	8	11	12
L_{α_1}	2.293	2.697	8.398	8.652
	100	100	100	100
L_{α_2}	2.289	2.692	8.335	8.586
	11	11	11	11
L_{β_1}	2.395	2.834	9.672	10.010
	53	52	67	66
L_{β_2}	2.518	3.001	9.962	10.275
	5	10	21	22
L_1	2.016	2.376	7.388	7.604
	5	4	5	5
L_{γ_1}	2.623	3.144	11.286	11.6854
	3	5	13	13
M_{α_1}			1.775	1.842
			100	100

The following figures (4 and 5) show graphically the information from the previous table. As can be seen from the table and figures, the strongest lines are K_{α_1} and L_{α_1} , followed by K_{α_2} and L_{β_1} , which we expect to reach the sample because of the high energies. Also M_{α_1} for W and Re, but the energy of this peak is extremely low ~ 1.8 keV and it will be removed with the exit window (inherent filtration) of X-ray tube and additional filtration placed after.

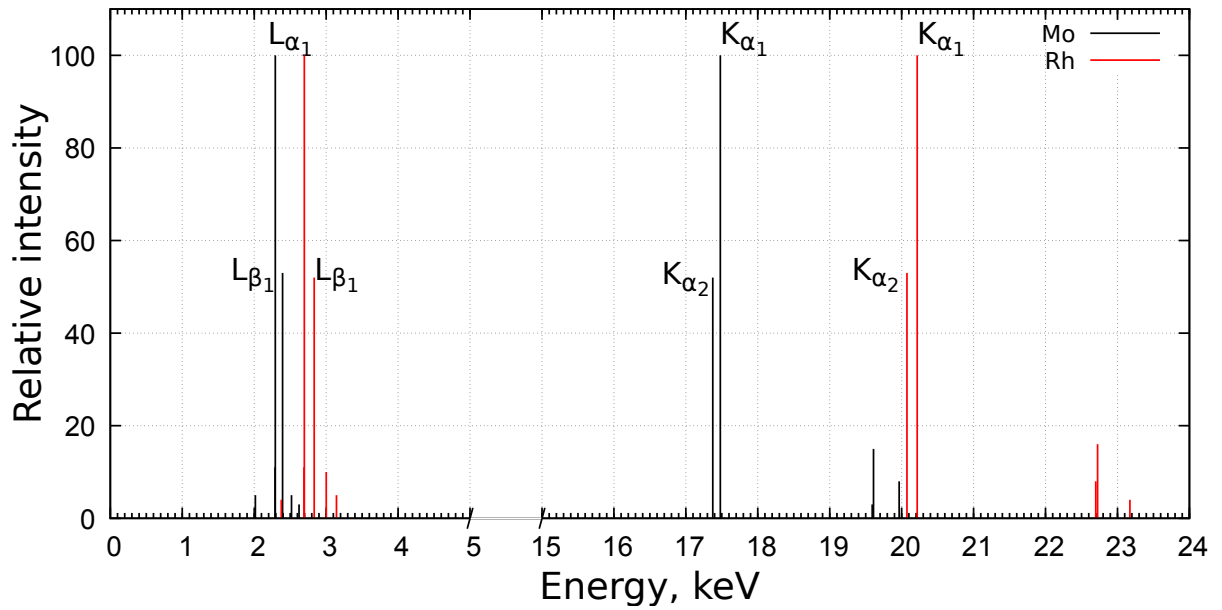


Figure 4: Characteristic lines for the Mo and Rh elements

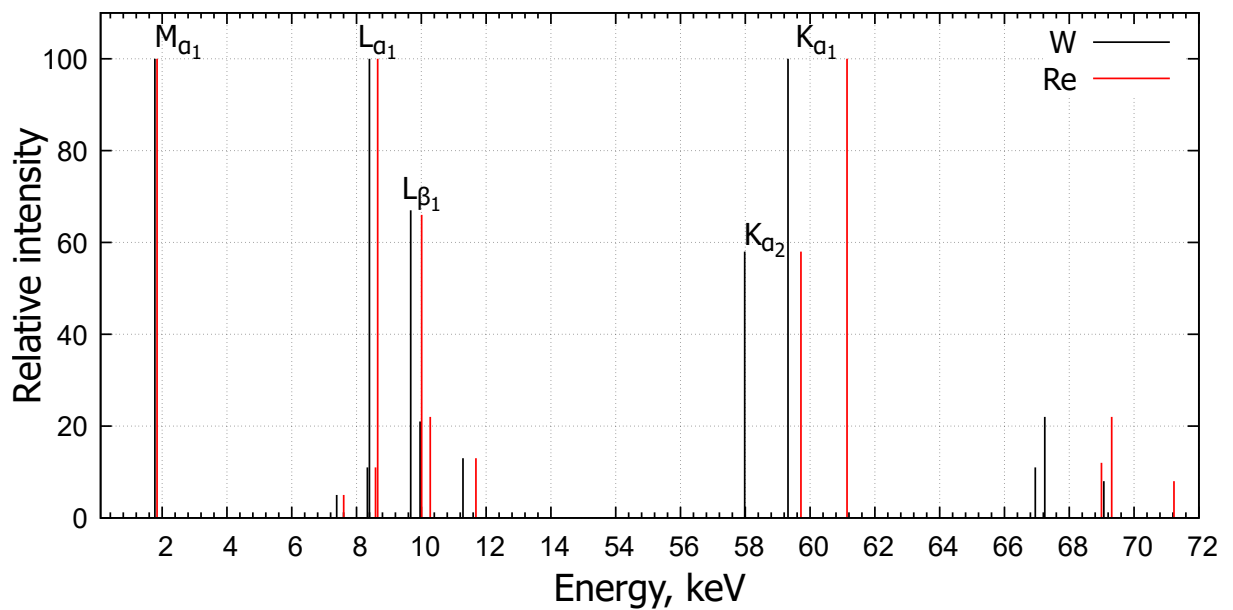


Figure 5: Characteristic lines for the W and Re elements

1.3 The basic interactions of photons with matter

The interactions of radiation such as photons are stochastic and obey the laws of chance. We can understand this process simply by considering a single photon to be incident on a slab of material of area A that contains one target of cross-sectional area σ . The probability of the photon interacting with the target will be the ratio of the two areas: σ/A [4, p. 12].

Next, let us say that there are N_p photons and that they are randomly directed at area A , and further, that area A contains n targets, each with area σ . It is easy to see that the expected number of interactions ΔN_p between photons and targets will be:

$$\Delta N_p = N_p(n\sigma/A) \quad (4)$$

Another way of stating this is that the probability of a projectile making a hit is $n(\sigma/A)$, which is just the fraction of the area that is blocked off by the targets. Now suppose that we change the geometrical description a little and we let the targets be atoms. Their cross-section would be an atomic cross-section. This would not be an actual area of the atom but would be an effective area for the interaction between the photon and the atom that is being considered. Cross-sections are frequently represented by the symbol σ and conventionally expressed in a unit of area called the barn ($1 b = 10^{-24} \text{cm}^2$).

There are four fundamental X-ray interactions that need to be considered; each can be associated with a specific cross-section: $\sigma_{\text{ph.effect}}$ is used to signify the cross-section for a photon to interact with an atom by the photoelectric effect, σ_{coh} is used to represent the cross-section for interaction by coherent scattering (Rayleigh scattering), σ_{incoh} for incoherent scattering (Compton scattering) and σ_{pair} for pair and triplet production. The first three of these interactions are important in the typical X-ray energy range (up to about 300 keV), whereas pair and triplet production only exists at much higher energies (starting from ~ 1 MeV). To summarize the processes explained before in one term is usually used the total cross-section, which takes into account these processes (excluding the last one):

$$\sigma_{\text{tot}} = \sum_i \sigma_i = \sigma_{\text{ph.effect}} + \sigma_{\text{incoh}} + \sigma_{\text{coh}} \quad (5)$$

1.3.1 Attenuation coefficients

The previous paragraph has been concerned with the interaction of photons with individual atoms, but it is also necessary to consider the macroscopic behaviour of photons traversing matter. For this purpose, linear and mass attenuation coefficients are used, which are simply related to the total cross-section(σ_{tot}). Photons may undergo more than one interaction as they pass through the material. For example, an initial scatter interaction might be followed by a second scattering process, which in turn might be followed by a third scatter, photoelectric absorption or no further interactions, with the photon leaving the material. Linear and mass attenuation coefficients give information about the passage of primary photons through the specific material. The radiation field at depth in the medium will also include scattered photons, which also contribute to the dose within the medium. The exit beam from the material will also comprise both primary and scattered photons.

Consider a thin uniform slab of material of thickness dx , which is irradiated with a beam of photons incident normally on the slab. Individual photons may pass through the slab without interacting, or they may be absorbed or they may be scattered. From the discussion in the beginning of subsection 1.3, it follows that the probability that an individual photon will interact in this thin section is given by: $N_a\sigma_{\text{tot}}dx$

Where N_a is the number of interaction centres (atoms) per unit volume and σ_{tot} is the total interaction cross-section per atom. The quantity $N_a\sigma_{\text{tot}}$ is known as the linear attenuation coefficient and is usually denoted by μ . For scattering by atoms, N_a may be calculated from the Avogadro constant, N_A , the atomic weight, A_r , and the density, ρ , so that:

$$\mu = N_a\sigma_{\text{tot}} = \frac{1000N_A\rho\sigma_{\text{tot}}}{A_r} \quad (6)$$

This expression is in SI units, so that the dimensions of μ are m^{-1} .

Now consider a thick slab of material and let Φ represent the number of photons, per unit of area, that have not interacted in the slab after passage through thickness x (see fluence in the subsection 1.4.1). The expected change, $d\Phi$, after passage through a further thickness dx is given by:

$$d\Phi = -\Phi\mu dx \quad (7)$$

Where the negative sign is used to signify that Φ is decreasing. Integration of the last equation gives:

$$\Phi = \Phi_0 e^{-\mu x}, \quad (8)$$

where Φ_0 is the initial value of the fluence. This is the equation describing the exponential attenuation of a photon beam. It is known as Beer-Lambert law. It should be noted that it describes the number of photons that have not interacted, also known as primary photons.

The linear attenuation coefficient μ is dependent on density, which in turn is dependent on the physical state of the material. As a consequence, μ is not a suitable quantity, and the related quantity μ/ρ , which is independent of density, is used instead. This quantity is known as the mass attenuation coefficient and its dimensions are square metres per kilogram m^2/kg . It should be noted that in most data compilations the mass attenuation coefficients are given in units of square centimeters per gram cm^2/g because historically they have been expressed in this way and this provides numbers that are convenient to manipulate.

An energy-related photon interaction coefficient is the mass energy-transfer coefficient, μ_{tr}/ρ , which accounts for the transfer of photon energy to the electrons

produced in the different interactions. It is defined as:

$$\mu_{\text{tr}}/\rho = \frac{N_A}{M} \sum_j f_j \sigma_j \quad (9)$$

Where, for each interaction type j , the coefficient f_j represents the mean fraction of the photon energy which is transferred to the kinetic energy of the electrons produced. N_A is the Avogadro constant and M is the molar mass of the material. The amount of energy transferred which is deposited locally is given by the mass energy-absorption coefficient, μ_{en}/ρ . Depending on the photon energy a fraction of the energy transferred can escape the local volume; this is given by the radiative fraction g , defined as the fraction of the kinetic energy of the generated electrons which is lost in radiative processes such as bremsstrahlung, fluorescence, etc. The two-photon interaction coefficients are related by:

$$\mu_{\text{en}}/\rho = (1 - g) \mu_{\text{tr}}/\rho \quad (10)$$

They convey the concept of photons being particles whose energy deposition to matter is indirect, as secondary electrons are created first by photon interactions, they are given a certain amount of energy, and this energy is subsequently deposited in matter through successive electron interactions.

Mass attenuation coefficients and mass energy transfer or absorption coefficients for compounds and intimate mixtures can be obtained by a weighted summation of the coefficients of the constituents:

$$\mu/\rho = \sum_i w_i (\mu/\rho)_i \quad (11)$$

where w_i are the normalized weight fractions of the elements i (or mixture components i) present in the absorber.

We now consider the three distinctly different mechanisms by which photons may interact with matter. They all compete, in that in any beam of photons they may all occur, each according to its individual probability. The total mass attenuation coefficient is therefore the sum of all the individual mass attenuation coefficients and, using Eq. (6), we obtain:

$$\mu/\rho = \mu_{\text{ph.effect}}/\rho + \mu_{\text{incoh}}/\rho + \mu_{\text{coh}}/\rho = \frac{1000N_A(\sigma_{\text{ph.effect}} + \sigma_{\text{incoh}} + \sigma_{\text{coh}})}{A_r} \quad (12)$$

The value of each attenuation coefficient will depend on the photon energy and the atomic number of the material. For example, the next figures show the cross sections (mass attenuation coefficients) for water (Fig 6) and air (Fig 7) for photon energies in the region from 1 keV to 300 keV.

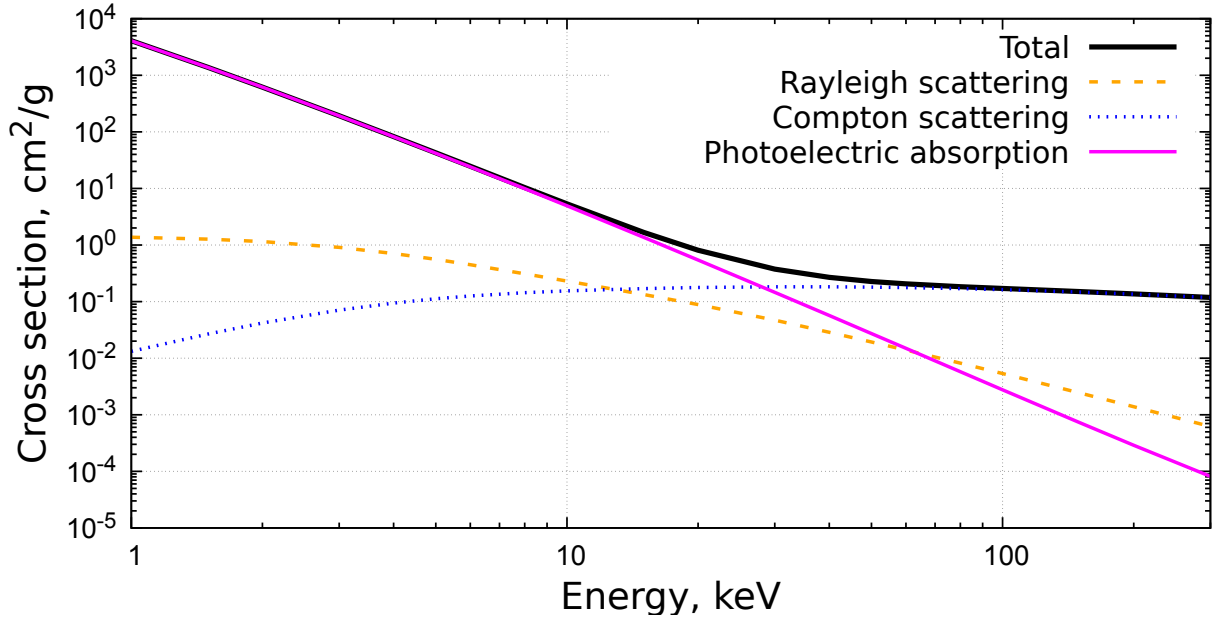


Figure 6: Cross sections of water for each mechanism of interactions

As can be seen from figures, the photoelectric interaction makes the dominant contribution to the total interaction cross-section at the lowest energies. The steep decrease at the lower photon energies is characteristic of the photoelectric effect and ends when incoherent (Compton) scattering becomes dominant, and remains so for the rest of the range. The crossover position for these two interactions depends on the atomic number, but for water is about 30 keV and for air is about

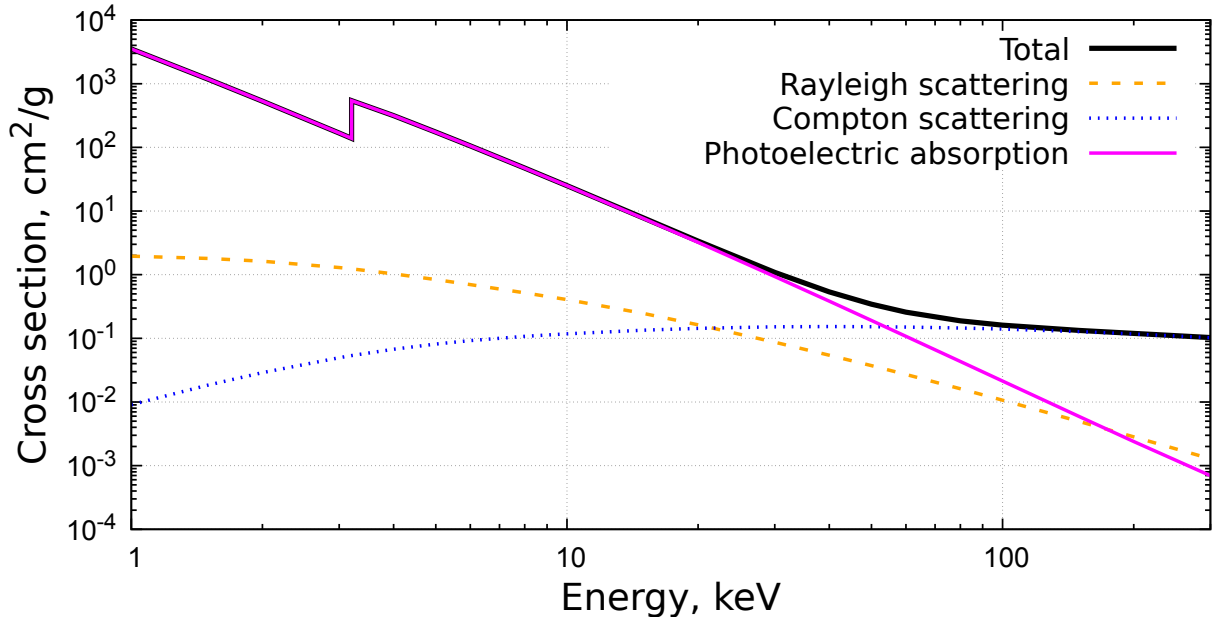


Figure 7: Cross sections of air for each mechanism of interactions

60 keV [4].

In the following subsections, we will explain some specifics of the different mechanisms of photon interaction with matter.

1.3.2 Photoelectric effect

In the photoelectric effect, the incident photon interacts with an atom, which is left in an excited state. The excess energy is released by the ejection of one of the electrons bound to the nucleus. This electron, called a photoelectron, leaves the atom with kinetic energy:

$$T_e = h\nu - E_s \quad (13)$$

Where T_e is the electron kinetic energy, h is Planck's constant, ν is the photon frequency and E_e is the binding energy of the electron shell from which the electron came.

The energy transferred to the recoiling atom is very small and can be neglected. The photoelectric effect can only take place if the photon energy, $h\nu$, exceeds the binding energy of the electron in that shell. The most probable electron

shell to lose an electron is the one that satisfies this constraint and also has the highest binding energy. Although this seems like a rather simple process, calculation of the probability of the interaction is very complicated and quantum mechanics is required. This is because it involves the wave function of the whole atomic electron cloud and these functions are available only for relatively simple atoms [1].

1.3.3 Rayleigh scattering

In the previous section, we discussed that in the photoelectric process, most of the photon's energy is converted into kinetic energy, and only a small fraction appears as characteristic scattered radiation. Here, we deal with a scattering process in which no energy is converted into kinetic energy, and everything is scattered. The process can be understood if we think of an electromagnetic wave of wavelength λ passing over the atom. The electromagnetic wave has an oscillating electric field associated with it that sets up a momentary vibration in the atom. These oscillating electrons emit radiation of the same wavelength, λ , as the incident radiation. This is exactly the same process that occurs in the transmitter of a radio station, where electrons are forced to oscillate, and the energy is radiated as a radio wave. The scattered waves from electrons within the atom combine with each other to form the coherent scattered wave. Scattering is a cooperative phenomenon and is therefore called coherent scattering. [2, p.149]

1.3.4 Compton scattering

Under certain circumstances, electrons can scatter independently; this is called incoherent scattering or Compton scattering. Some energy is scattered and some is transferred to kinetic energy. It is the most important interaction mechanism in tissue-like materials. For this type of interaction, we must consider the quantum nature of radiation and think of the electromagnetic wave as a stream of

photons with energy $h\nu$ and momentum $h\nu/c$. The process can be understood if we think of the photon colliding with a free electron. This puts the electron in motion with energy E at an angle θ , carrying away part of the energy, while the rest of the energy is carried away by a photon with energy $h\nu'$ at an angle ϕ . The collision energy is conserved so that:

$$h\nu = h\nu' + E \quad (14)$$

This equation shows that ν' must be less than ν (and the scattered waves must be of longer wavelength, λ' , than the incident radiation, λ). In a Compton collision, some energy is absorbed (recoil electron energy) and some is scattered in each collision. Because momentum is also conserved, the scattering angle θ of the electron is uniquely determined if the scattering angle ϕ is known.

Here we describe the process qualitatively. If the photon makes a direct hit on the electron, the electron will travel straight forward ($\phi = 0$), and the scattered photon will be scattered straight back with $\theta = 180^\circ$. In this type of collision, the electron will maintain its maximum energy and the scattered photon its minimum energy. If, on the other hand, the photon makes a grazing hit with the electron, the electron will emerge nearly at right angles ($\phi = 90^\circ$) and the scattered photon will go almost straight forward ($\theta = 0^\circ$). In this collision, the electron receives almost no energy and the scattered photon has escaped with nearly all the energy of the incident photon. All manner of intermediate collisions are possible.

The Compton process explained before is assuming the electron is free or unbound. Strictly speaking, no electron is free since even the outer electrons of the atom are bound by a few electron volts. However, these binding energies are a small fraction of the photon energy, so for tissues, the electron may be considered free. [2, p.151]

1.4 Basic dosimetry and beam-quality characterization

1.4.1 Field and dosimetry quantities

A radiation field is a group of particles, that is, photons, electrons, positrons, protons, neutrons, etc., each having radiant energy and moving in a certain direction. Given a radiation field consisting of N particles, the field quantity fluence is defined as the number of particles dN incident on a sphere of cross-sectional area da :

$$\Phi = \frac{dN}{da}, \quad (15)$$

with unit cm^{-2} . The concept of a sphere conveys the idea of an area which is perpendicular to the direction of each particle [1]. This definition of fluence is more accurate than the used in previous sections.

A related field quantity is the energy fluence, defined as the radiant energy incident on a sphere of cross-sectional area da , which, for example, can be photons, written as:

$$\Psi = E\Phi, \quad (16)$$

with units J/cm^2 , where E is the energy of the photons. The field quantities fluence and energy fluence can be expressed as distributions with respect to energy as:

$$\Phi_E = \frac{d\Phi}{dE}, \quad \Psi_E = \frac{d\Psi}{dE}, \quad (17)$$

where $d\Phi$ is the fluence of photons with energy between E and $E + dE$ and $d\Psi$ its energy fluence. The two quantities differential in energy, Φ_E and Ψ_E , are commonly referred to as fluence spectrum and energy-fluence spectrum, respectively. Their respective integrals lead to the total quantities in terms of E . For the latter, they are:

$$\Phi = \int \Phi_E dE, \quad \Psi = \int \Psi_E dE. \quad (18)$$

The dosimetry of photons with energies up to about 300 keV is governed by the quantity kerma, which accounts for the transfer of the kinetic energy of photon-produced electrons to a volume of material. Kerma is the acronym for kinetic energy released per unit mass and has the unit of gray (Gy). It can be shown that in a given medium, kerma is related to the field quantities fluence and energy fluence through:

$$K = E\Phi_{\text{med}} \left[\frac{\mu_{\text{tr}}(E)}{\rho} \right]_{\text{med}} = \Psi_{\text{med}} \left[\frac{\mu_{\text{tr}}(E)}{\rho} \right]_{\text{med}}, \quad (19)$$

where E is the photon energy, Φ is the photon fluence in the medium, and $\frac{\mu_{\text{tr}}(E)}{\rho}$ is the photon mass energy-transfer coefficient of the medium at the energy E .

When only a fraction of the energy transferred to the volume under consideration is locally deposited, the collision (or electronic) kerma describes the component of the kerma resulting from such energy deposition:

$$K_{\text{col}} = K(1 - g), \quad (20)$$

where g is the radiative fraction defined above, see Eq. (10). K_{col} can also be expressed in terms of fluence and energy fluence:

$$K_{\text{col}} = E\Phi_{\text{med}} \left[\frac{\mu_{\text{en}}(E)}{\rho} \right]_{\text{med}} = \Psi_{\text{med}} \left[\frac{\mu_{\text{en}}(E)}{\rho} \right]_{\text{med}}. \quad (21)$$

It should be emphasized that at the photon energies considered for our work, the radiative fraction is practically negligible for light materials and most human tissues. For example, for 300 keV the mean energy of Compton produced electrons is about 80 keV, for which the radiation yields in water, air, muscle, and bone are

within 0.05%–0.07%. Hence, it is reasonable to assume that $\mu_{en}/\rho = \mu_{tr}/\rho$ and $K = K_{col}$. Additionally, when charge-particle equilibrium exists, the absorbed dose in the medium, D , i.e., the sum of all the energy deposits (energy imparted) in a mass of matter dm divided by it, is numerically equal to the kerma, hence:

$$D \stackrel{\text{CPE}}{=} K = E\Phi_{\text{med}} \left[\frac{\mu_{tr}(E)}{\rho} \right]_{\text{med}} \stackrel{g \approx 0}{=} E\Phi_{\text{med}} \left[\frac{\mu_{en}(E)}{\rho} \right]_{\text{med}} \quad (22)$$

The relationships above refer to mono-energetic photons. They can be generalized to a fluence spectrum or an energy-fluence spectrum of maximum photon energy E_{max} as:

$$K = \int_0^{E_{\text{max}}} E(\Phi_E)_{\text{med}} \left[\frac{\mu_{en}(E)}{\rho} \right]_{\text{med}} dE = \int_0^{E_{\text{max}}} (\Psi_E)_{\text{med}} \left[\frac{\mu_{en}(E)}{\rho} \right]_{\text{med}} dE \quad (23)$$

1.4.2 Percentage Depth Dose

The percentage depth dose (PDD) is the ratio of the dose at point A (D_A) to the dose at point B (D_B), both being within the sample. It is expressed as a percentage thus:

$$\text{PDD} = \frac{D_A}{D_B} \cdot 100, \quad (24)$$

This percentage dose depends on the depth of the sample, the width of the beam, the distance from the source to it and also on the quality of the radiation. It is convenient to relate doses to a reference point other than B, e.g B_r which can be at depth 100 mm. When this is done percentage depth doses can exceed 100 and are often referred as relative depth doses [2, p.338]. Percentage dose may be measured in different ways. One way is placing various detectors at different depth, to get the information in each of these point and then compare with a reference point

commonly placed on the surface of the sample.

1.4.3 Beam quality characteristics

Photon spectra given in terms of fluence or energy fluence are the most suitable descriptors of the characteristics of a photon beam, enabling the determination of relevant dosimetric quantities. However, detailed spectra are often not available or their use is not practical in routine work. Simpler calculated or experimental parameters have been developed over the years that have become widely accepted by the X-ray community to characterize the so-called beam quality

When the photon spectral distribution is available, either by measurement or by calculation, a commonly used parameter to characterize the quality of an X-ray beam is the mean energy of the spectrum. This is, however, not a unique specifier and has certain weaknesses. Firstly, it is possible for two different spectra to have identical or very similar mean energy. Secondly, and more important, depending on the type of spectrum available, given in terms of fluence or of energy fluence, the mean energy is defined differently. The field quantity in which a spectrum is given should always be stated. Hence, for a fluence spectrum, the fluence-weighted mean energy is defined as:

$$\bar{E}_\Phi = \frac{\int_0^{E_{\max}} E \Phi_E dE}{\int_0^{E_{\max}} \Phi_E dE}, \quad (25)$$

which is the ratio of total energy fluence to total fluence, Ψ/Φ . For an energy spectrum, the energy-fluence-weighted mean energy is

$$\bar{E}_\Psi = \frac{\int_0^{E_{\max}} E \Psi_E dE}{\int_0^{E_{\max}} \Psi_E dE} = \frac{\int_0^{E_{\max}} E^2 \Phi_E dE}{\int_0^{E_{\max}} E \Phi_E dE}. \quad (26)$$

In radiation protection and diagnostic and interventional radiology applications, a third option has become frequently used, particularly at standards dosimetry laboratories. The mean energy is stated in terms of air kerma, so that in analogy with \bar{E}_Φ and \bar{E}_Ψ above, the air-kerma-weighted mean energy is defined as

$$\bar{E}_{K_{\text{air}}} = \frac{\int_0^{E_{\text{max}}} EK_{\text{air},E} dE}{\int_0^{E_{\text{max}}} K_{\text{air},E} dE} = \frac{\int_0^{E_{\text{max}}} E^2 \Phi_{E,\text{air}} [\mu_{\text{en}}(E)/\rho]_{\text{air}} dE}{\int_0^{E_{\text{max}}} E \Phi_{E,\text{air}} [\mu_{\text{en}}(E)/\rho]_{\text{air}} dE}, \quad (27)$$

where $K_{\text{air},E}$ refers to the air kerma spectrum, obtained at each energy E by calculation from Φ_E or Ψ_E distributions. The air-kerma-weighted mean energy $\bar{E}_{K_{\text{air}}}$ is often referred to as the dose-weighted mean energy, simply denoted by E_D or \bar{E}_D . It should be emphasized, however, that this modality of mean energy depends on the data set selected for the mass energy-absorption coefficients of air. The $\bar{E}_{K_{\text{air}}}$ modality can then be said to be less robust than \bar{E}_Ψ and \bar{E}_Φ .

Mean energy is often used to obtain from a lookup table a mean interaction coefficient which is assumed to correspond to the spectrum at hand, e.g., $\mu(\bar{E}_\Psi)$ for the lineal attenuation coefficient of the energy-fluence-weighted mean energy. An accurate mean coefficient value should, however, be obtained by weighting $\mu(k)$ values with the detailed spectrum, which results in the energy-fluence-weighted average coefficient:

$$\bar{\mu}_\Psi = \frac{\int_0^{E_{\text{max}}} \mu(E) \Psi_E dE}{\int_0^{E_{\text{max}}} \Psi_E dE}, \quad (28)$$

Usually different from $\mu(\bar{E}_\Psi)$. Similar mean coefficient values can be formulated and conclusions drawn for $\mu_{\text{en}}(\bar{E}_\Psi)/\rho$ and $\overline{(\mu_{\text{en}}/\rho)}_\Psi$, or for $\mu_{\text{en}}(\bar{E}_\Phi)/\rho$ and the fluence-weighted average coefficient $\overline{(\mu_{\text{en}}/\rho)}_\Phi$, etc.[1, p.42]

The quality of an X-ray beam is most often characterized through suitable attenuation measurements in a given material, usually aluminium and copper. For this purpose, the air kerma of x rays transmitted by different thicknesses of the selected material is measured under narrow-beam geometry conditions,normaliz-

ing the results to the air kerma measured without attenuation material. The “HVL”, half-value layer, can also be determined by calculation when the incident spectrum is known, e.g. using an iterative procedure. Material thicknesses corresponding to different attenuation fractions define n-value layers. The first half-value layer, HVL_1 , is defined as the thickness of material required to reduce the air kerma to 50% of its initial value without attenuation material. The second half-value layer, HVL_2 , is the additional material thickness necessary to reduce the initial air kerma to 25% of the initial value. For X-ray beams below about 100 kV, HVLs are typically expressed in millimetres of high-purity aluminium; above 100 kV, HVLs are usually given in millimetres of high-purity copper. There is a region of overlap around 100 kV where HVLs can be given in thickness of any of the two materials.

The ratio HVL_1 / HVL_2 defines the homogeneity index h_i , which provides a sense of the spectral width and is unity for mono-energetic photons.

A related quantity used in X-ray beam quality specification is the effective energy, defined as the energy of a mono-energetic photon having the same HVL_1 as the beam whose quality is to be specified. The effective energy does not provide more information than HVL_1 , but can be useful to describe a heavily filtered beam with a spectrum approaching the shape of a monoenergetic beam. Note that its precise value does depend on whether the HVL_1 value is specified in aluminium or copper [1, p.44].

2 Materials and methods

The objective of this work was to become familiar with the technical equipment at the LRB, JINR, by conducting a dosimetric analysis using a specially developed mouse phantom irradiated on the SARRP machine from the laboratory. We evaluated the percentage depth dose distribution through several methods. First, we obtained initial results from MuriPlan, the treatment planning system associated with the SARRP irradiation machine. These were followed by measurements using dosimetric films, and finally, we performed a Monte Carlo simulation to replicate the experimental setup and validate the results.

In this section we will discuss, in general, methods that we used in our experiment, comment on the materials, installations involved in the process, and in the end we will describe the whole experiment workflow.

2.1 General information and capabilities of SARRP facility

The equipment for irradiation that we used, was a SARRP machine, it stands for Small Animal Radiation Research Platform (see Figure 8). It is used in radiobiology science research for image-guided micro irradiation. This platform allows the acquisition of a cone beam computed tomography (CBCT) image for determining the most accurate depth for treatment. The accurate treatment time and can be initiated within the software.

The SARRP standard components include:

- X-ray Generator.
- Cooling System and Safety Interlocks.
- X-ray (MP1) Controller.



Figure 8: SARRP facility at the LRB JINR

- 225 kV X-ray Tube.
- SARRP Interface and PC.
- 360-degree Rotating Gantry.
- Flat Panel Detector.
- Copper and Aluminum Filter.
- Flat bed.
- Lasers and Webcam.

We also used some of the optional components of the machine, such as, the specialized collimators. In our case the selected collimators had a circular orifice and diameter sizes were: 1 mm and 10 mm.

The SARRP can generate X-rays up to 225 kV with a mA range of 0 to 30 mA, at a maximum power limit of 3 kW. The X-ray tube assembly consists of a

Table 2: Main characteristics of the SARRP X-ray tube

Nominal X-ray tube voltage	225 kV
Focal spot size	Fine (D = 1.0 mm) Broad (D = 5.5 mm)
Inherent filtration	0.8 ± 0.1 mm Be
Target material	Tungsten
Target angle	20°
Radiation coverage	40°

unipolar X-ray tube with a cooled anode at ground potential and a high voltage receptacle socket. The X-ray tube is cooled through water hose connectors. In the Table 2 the main characteristics of the X-ray tube are shown.

SARRP Control Software is a fully integrated software interface that controls X-rays, imaging, and mechanics. As an X-ray control software, it allows the computer to talk to the X-ray controller (MP1), which is a microprocessor controlled control panel to be used in conjunction with X-ray Generator to regulate it. When in X-ray control mode, the software will not allow you to turn X-rays on until all the safety conditions are met [6].

This SARRP facility also comes with a associated software for treatment planning called MuriPlan. MuriPlan is a pre-clinical treatment planning system enabling users to develop and execute treatment plans quickly and easily. It allows the user to load an existing cone-beam computed tomography (CBCT) reconstruction or acquire a new CBCT scan. Using a Graphic Processing Unit (GPU) for image reconstruction dramatically decreases the amount of time spent with the subject under anesthesia. The CBCT is displayed in slices along three different axes and can also be viewed as a three dimensional reconstruction, like it is shown in Figure 9.

The user has tools to create contours for organs at risk and tumor volumes. Using this data, researchers can create a treatment plan with beams or arcs that mimic clinical practice. MuriPlan offers two methods to calculate the dose, a high accuracy Monte Carlo (MC) algorithm and a high-speed superposition-

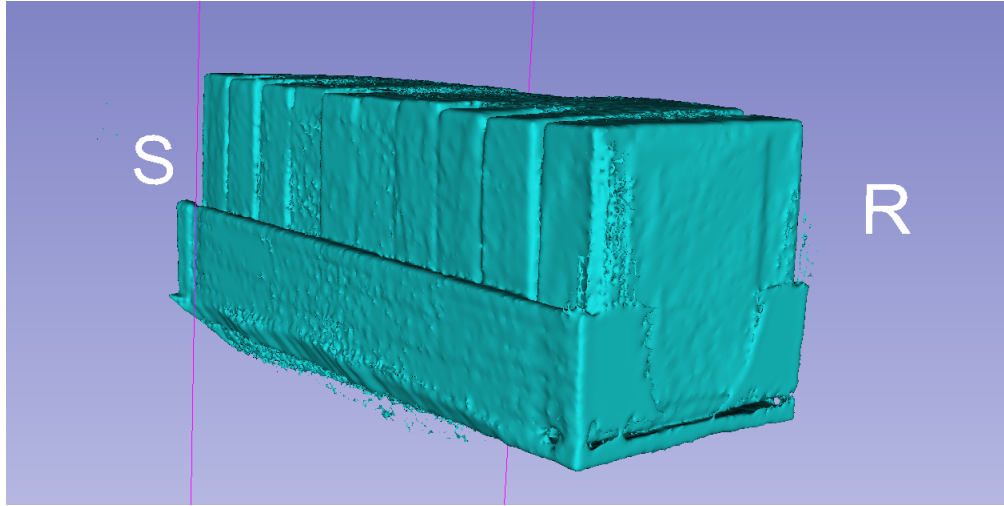


Figure 9: MuriPlan reconstruction of the manufactured mouse phantom for the experiment

convolution (SC) algorithm implemented on the GPU, in our case we used the latter one. To determine plan quality and accuracy, MuriPlan can compute isodose lines and the user can evaluate the dose distribution in a Dose Volume Histogram (DVH). All plan parameters can be saved for other subjects, consequent treatments or as a text file to report the irradiation from a specific subject. The treatment plans can be easily communicated to the SARRP software for the beam delivery [7].

2.2 Mouse phantom manufacturing

In order to make a simplified recreation of a mouse for the experiment, the first thing that should be taken into account is the mouse average dimensions, normally the its length goes from 6 to 11 cm [8], in the lab rats and mice are used for various research and sizes changes in the range from 6 to the maximum of 20 cm (for rats). So, our phantom was designed to be extendable to represent different lengths of the animal. For this purpose, more than 12 small pieces of 1 cm each were cut as shown in figure 10 to place detectors in between each small piece. In actual experiment we used 10 pieces. The material used for the pieces is called PMMA, a water equivalent plastic, with density of 1.190 g/cm^3 , mean atomic number \bar{Z} of 5.85 and elemental composition (fraction by weight): H — 0.0805, C —

0.5998, O — 0.3196 [9, p.42]. Radiology water equivalence is an important quality of solid phantom materials proposed to be used for dosimetric applications that rely on the attenuation and scattering characteristics of water. It is accepted a quantification of phantom water-equivalence, describing the phantom as water equivalent if it does not introduce uncertainties greater than 1% in the calculation of absorbed dose [10].

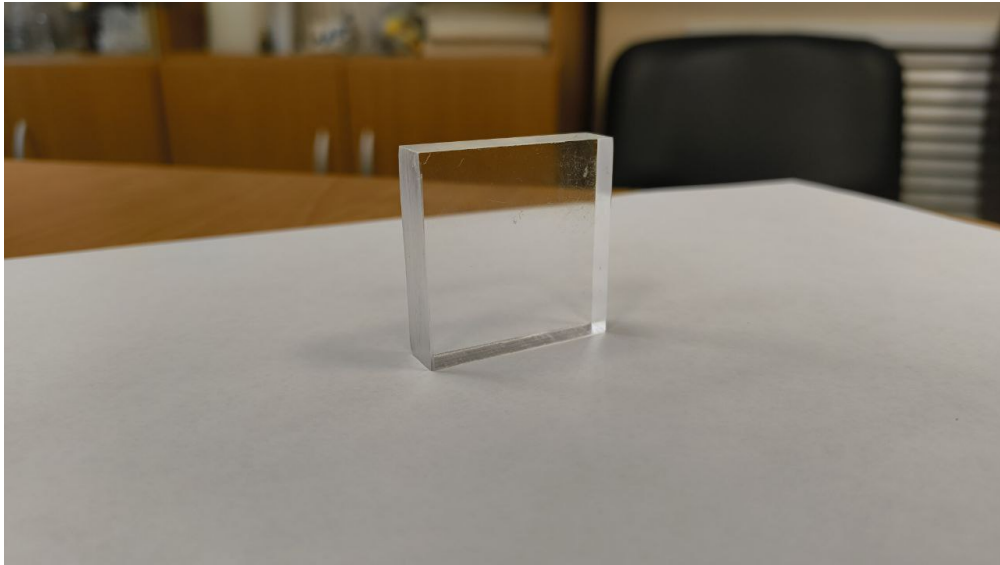


Figure 10: Mouse phantom piece

To create a holder for our pieces, we needed to use an accurate object and utilize a material that was water equivalent also, to not disturb our experiment. Normally to create a 3D object a CAD software is used, CAD stands for Computer Aided Design, which can be define as the use of computers systems to assist in the creation, modification, analysis or optimization of a design. CAD output is often in the form of electronic files for print, machining, or other manufacturing operation [11]. The CAD software used was Autodesk Inventor, it is 3D CAD software that provides mechanical design, documentation, and simulation tools. It has a powerful blend of parametric, direct, freeform, rules-based design, integrated tools for design various 3D models. Also a Powerful Model-Based Definition for embedding manufacturing information directly in the 3D model [12]. After creating the model of our holder, it was exported and then process by the 3D printer of

the laboratory which is a FlyingBear ReBorn 2. This printer uses the most popular deposition modeling which is called Fused Deposition Modeling or FDM for short, it is a material extrusion method of additive manufacturing where materials are extruded through a nozzle and joined together to create 3D objects. A typical FDM 3D printer takes a polymer-based filament and forces it through a heated nozzle, which melts the material and deposits it in 2D layers on the build platform. While still warm, these layers fuse with each other to eventually create a three-dimensional part [13]. The plastic used is also a water equivalent one, called PETG [14], it stands for Polyethylene terephthalate glycol. This material has density of 1.3 g/cm^3 approximately and chemical composition is $(\text{C}_{10}\text{H}_8\text{O}_4)_n$ [15]. The figure 11 shows the result of the manufacturing process discussed.

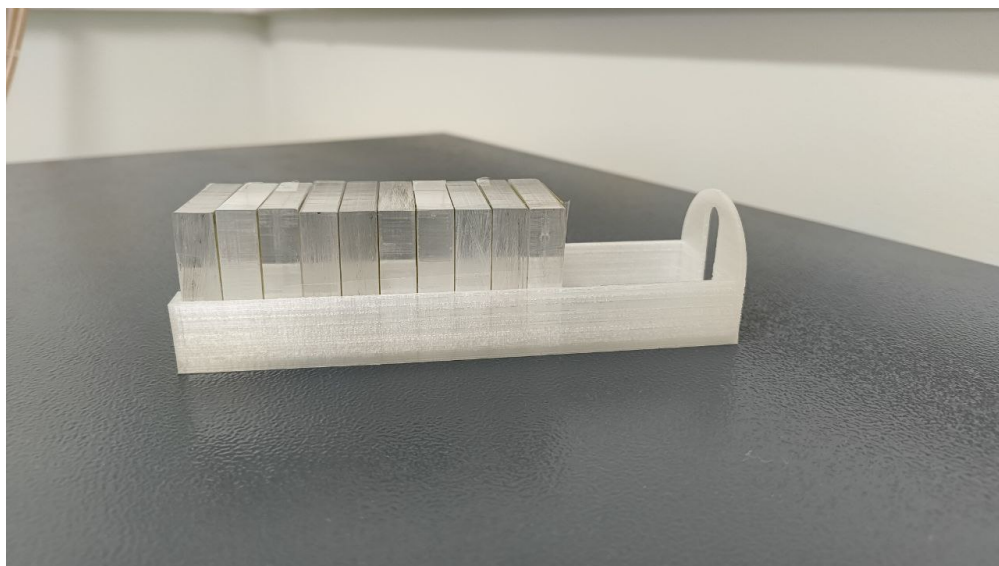


Figure 11: 3D printed holder with phantom pieces inside

2.3 Film dosimetry

In the field of dosimetry there are various options of dosimeters, i.e solid-state ones, ion chambers and also film dosimeters. There are two distinct types of film: radiographic film and radiochromic film. Radiographic film is similar to that used in older radiography applications and requires chemical development. Chemical development adds cost and introduces significant variability in dose measure-

ment. Radiochromic film is self-developing via a polymerization reaction. This self-development feature has caused radiochromic film to largely supersede radiographic film for dosimetry purposes. In our work we used one common type of radiochromic film, Gafchromic EBT3. The mechanism, for dosimetry, begins when radiation incident on the active layer induces a polymerization reaction. As the active layer polymerizes, it becomes partially opaque in proportion to the incident dose. This process continues for several hours and the time between measurement and readout must be controlled. After 1-24 hours, the film is read out on a calibrated optical digitizer or flatbed scanner. Near immediate readout is possible but results in decreased measurement precision [16].

2.3.1 Gafchromic EBT3 films

Radiochromic films such as Gafchromic EBT3 are designed for the measurement of absorbed doses of ionizing radiation, representing a useful tool for dose verification of modulated treatment plans and general quality assurance of beams. EBT3 films provide several characteristics that make them suitable for different situations: high spatial resolution, weak energy dependence and near-tissue equivalence. Moreover, they are self-developing, as explained before, thus avoiding practical difficulties related to post-exposure treatments. The range of absorbed doses in which they best perform is from 0.2 Gy to 10 Gy. After 24h from irradiation, EBT3 can be scanned and the resulting image is analyzed thanks to a software to accomplish this task. These films are distributed in the standard size 8"x10" and boxed in packages of 25 sheets. Films are separated from one another by a piece of paper, and they are stored in a black envelope. It is recommended to keep the non-exposed sheets protected from sunlight and at room temperature (20°C - 25°C). Nevertheless they can be handled under artificial light without noticeable effects.

We used the whole sheet for our measures, but cutting smaller pieces is allowed, as long as it is kept the same orientation for every piece, this was our case.

They are made of three layers the active layer, nominally 28 μm thick, surrounded by two 125 μm matte-polyester substrates. The active layer contains the active component, a marker dye, stabilizers and other components to give the film its (almost) energy independent response. The thickness of the active layer will vary slightly between different production lots, as a consequence it is recommended that films for calibration and measures come from the same lot number. The polyester layers are designed to protect the inner active layer, making these films suitable for water immersion. Taking notes with a marker is also allowed. Moreover, the symmetrical structure allows for side-independent measures. When unexposed, EBT3 are yellow, then when the active component is irradiated, it reacts to form a blue colored polymer [17].

2.3.2 Preparation of Gafchromic EBT3 films for irradiation

Each film dosimetry system consists of three main components: the model of the film used, the scanning device, and the scanning protocol. The following equipment and accessories are used for radiochromic dosimetry:

- Radiochromic film EBT3
- Epson Perfection V750 Pro flatbed scanner
- A4 format transparent PET sheet, 0.5 mm thick
- A4 format transparent acrylic plexiglass sheet, 3 mm thick
- Paper guillotine or sharp scissors
- Permanent markers
- Dark envelopes, binders, folder, gloves

Before working with the film, it must be properly cut, labeled, scanning templates prepared, etc. After that, calibration is carried out for the necessary operating modes on the installations. All the film used in the work should be from the same batch; when switching to a new batch, recalibration is required.

A mandatory condition for the scanner is the ability to scan the film in transparency mode. There is a significant amount of literature data dedicated to working with various scanners [18–25]. For various reasons, the Epson Expression 10000-12000XL and Epson Perfection V700-850 are considered the best, so the Epson Perfection V750 Pro flatbed scanner was chosen for this work (see Figure 12), in transparency mode.



Figure 12: Epson Perfection V750 Pro flatbed scanner used for scanning films

The PET sheet is used to prepare templates for the films. The purpose of the template is to position the films along the central axis of the scanner in a fixed position, as literature data indicate that positioning the film at the sides can lead to measurement errors in intensity. The acrylic sheet is necessary to press the film against the glass, ensuring correct color transmission, which affects the determination of optical density. Figure 13 shows the placement of the template and the pressing glass on the scanner.

The paper guillotine (saber cutter) ensures proper cutting of the film, pro-



Figure 13: Template and acrylic glass for positioning the film on the scanner

viding a straight cut and minimizing impact on the edges, which affects the measurement of optical density. It is worth noting that regular scissors or a roller cutter do not achieve such a straight cut.

Labeling is done using permanent markers no thicker than 0.8 mm, which should not erase during use, under the influence of water or alcohol, as losing the number on the films would make them impossible to identify and correlate with the irradiation protocol.

Dark envelopes are necessary for storing the film in a dark place since exposure to light should be minimized. Binders allow convenient storage of cut film pieces intended for calibration.

The following software is used:

- Epson Scan 2 (film scanning)
- ImageJ (scan processing and fitting)

The EBT3 film is supplied in sheets of 8x10 inches (203x254 mm). For calibration, the sheets are cut into rectangles of 25x20 mm, as shown in figure 14. One sheet yields 100 films ready for irradiation. Landscape orientation is chosen

for cutting and subsequent scanning.

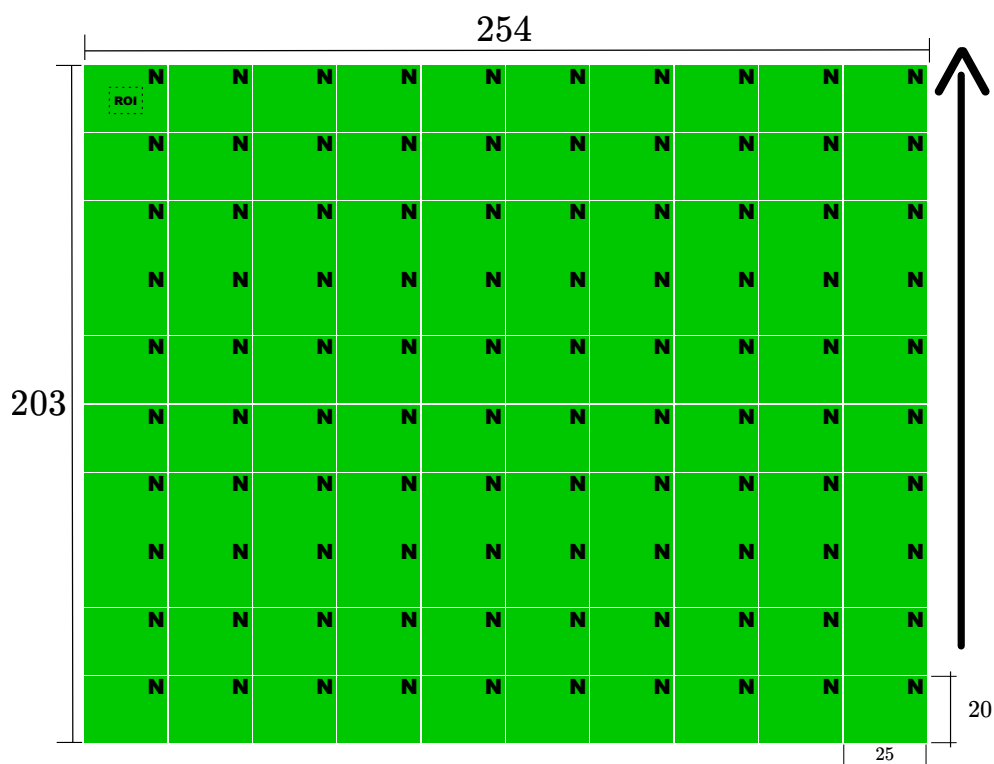


Figure 14: Diagram showing the process of cutting one 8x10 inch film sheet into 100 rectangles of 25x20 mm, with numbering indicated

It is important to maintain the orientation of the cut rectangles, as the active layer of the films is composed of the monomer LiPCDA, whose crystals have a rod shape with a thickness of about 2 μm and a length of 15 μm , oriented parallel to the short side of the sheet [24]. To maintain their orientation, the long side of the cut films should always be placed parallel to the scanner lamp; figure 14 shows the direction of the lamp movement during scanning with an arrow. The number is indicated in the upper right corner. Each number is recorded in the irradiation protocol on the installation, which allows correlating the results obtained with the irradiation conditions.

When cutting the film, it is also crucial to work in gloves and avoid touching the area where optical density readings will be taken, this area is referred to as ROI¹ (see figure 14). Fingerprints, cracks, and other defects on the film will affect the

¹Region of Interest

accuracy of intensity measurement and, ultimately, the absorbed dose.

Before scanning, ensure that the scanner glasses are free of contamination, and clean them if necessary. Place the appropriate scanning template. Insert the film into the template. Place the pressing glass on top. After that, you can start working with the scanner. To warm up the scanner lamp, it is necessary to perform 5 preliminary scans before the actual scanning. Additionally, before each scan, 3 intermediate scans are required to stabilize the scanner lamp's operation. The fourth scan is used for further analysis.

2.3.3 Gafchromic EBT3 films calibration process

The calibration process involves determining the relationship between the optical density and the absorbed dose of the radiochromic film. For this purpose, the film is irradiated with a set of pre-determined doses, which are established using an externally calibrated dosimeter. The optical density–absorbed dose values obtained are used to construct a calibration curve, allowing the recovery of absorbed dose values based on the optical density of films irradiated with an unknown dose.

The external dosimeter used to accurately determine the absorbed dose for a given quality of X-ray radiation, determined by tube voltage and filtration, is the PTW-UNIDOS E universal dosimeter with a Farmer Chamber Type 30010 ionization chamber. This dosimeter was pre-verified and calibrated at the VNIIFTRI for the following operating modes:

1. 130 kV + Al 0.5 mm
2. 130 kV + Al 1.0 mm
3. 130 kV + Cu 0.15 mm
4. 220 kV + Al 1.0 mm

5. 220 kV + Cu 0.15 mm

Each operating mode has its own X-ray quality, determined by the photon spectrum. The only one calibration curve can be used, because the manufacturers of EBT-3 film claim energy independence above 100 kV.

The dependence of film exposure on absorbed dose is usually expressed as the ratio of the measured optical density (OD) to the dose. To use the film for measuring an unknown dose, it is more convenient to plot the dose on a graph depending on the net optical density (netOD). The calibration curve is determined by fitting using the least squares method. The optical density is calculated based on the scanner readings as [26]:

$$\text{netOD} = \lg \frac{I_0 - I_\infty}{I_D - I_\infty}, \quad (29)$$

where I_0 is the intensity (pixel value) of the unexposed film (zero dose); I_∞ is the intensity of the overexposed film (dose an order of magnitude higher than the maximum used in irradiation); I_D is the intensity at dose D . The maximum pixel value in the selected scanner mode (48-bit, or 16-bit per channel) $I_{\max} = 2^{16} - 1$ corresponds to pure white light passing through without attenuation, and accordingly, the value $I_{\min} = 0$ indicates that all light is fully absorbed. These pixel values are obtained using the program ImageJ. The intensity values I are the average values read from the scanner over an ROI. The dose are fitted using the formula:

$$D_{\text{fit}} = a \cdot \text{netOD} + b \cdot \text{netOD}^n. \quad (30)$$

The fitting parameter n is not adjusted during the fitting process. Instead, the best value is selected within the range from 0.5–5, with a step size of 0.01.

The uncertainties are associated with the experimental measurement of netOD:

$$\sigma_{D_{\text{exp}}}(\%) = \frac{\sqrt{(a + b \cdot n \cdot \text{netOD}^{n-1})^2 \cdot \sigma_{\text{netOD}}^2}}{D_{\text{fit}}} \cdot 100, \quad (31)$$

and also with the parameters used for the selected fit:

$$\sigma_{D_{\text{fit}}}(\%) = \frac{\sqrt{\text{netOD}^2 \cdot \sigma_a^2 + \text{netOD}^{2n} \cdot \sigma_b^2}}{D_{\text{fit}}} \cdot 100. \quad (32)$$

Finally, the total dose uncertainty, measured using the above-described formalism, is:

$$\sigma_{D_{\text{total}}}(\%) = \frac{\sqrt{\text{netOD}^2 \cdot \sigma_a^2 + \text{netOD}^{2n} \cdot \sigma_b^2 + (a + b \cdot n \cdot \text{netOD}^{n-1})^2 \cdot \sigma_{\text{netOD}}^2}}{D_{\text{fit}}} \cdot 100. \quad (33)$$

After determining the form of the calibration curve, all results obtained in subsequent irradiation experiments are converted into dose. The following Figure 15 shows the calibration curve obtained using operational mode 130 kV + Al 0.5 mm on the CellRad X-ray irradiator at LRB JINR (date 07.06.2023).

2.4 Monte Carlo calculations for experiment verification

Monte Carlo is, in essence, a methodology to use sample means to estimate population means. Although Monte Carlo is inherently involved with the concept of probability, it can be applied, with much success, to problems that have no apparent connection with probabilistic phenomena. The methods are based on rigorous mathematics that began with the first statement of the law of large numbers, as enunciated by Jacob Bernoulli over 300 years ago. Monte Carlo is particularly valuable when considering multidimensional integrals, where it generally outperforms traditional quadrature methods. Significantly, it also can be applied to a great variety of problems for which the integral formulation is not posed ex-

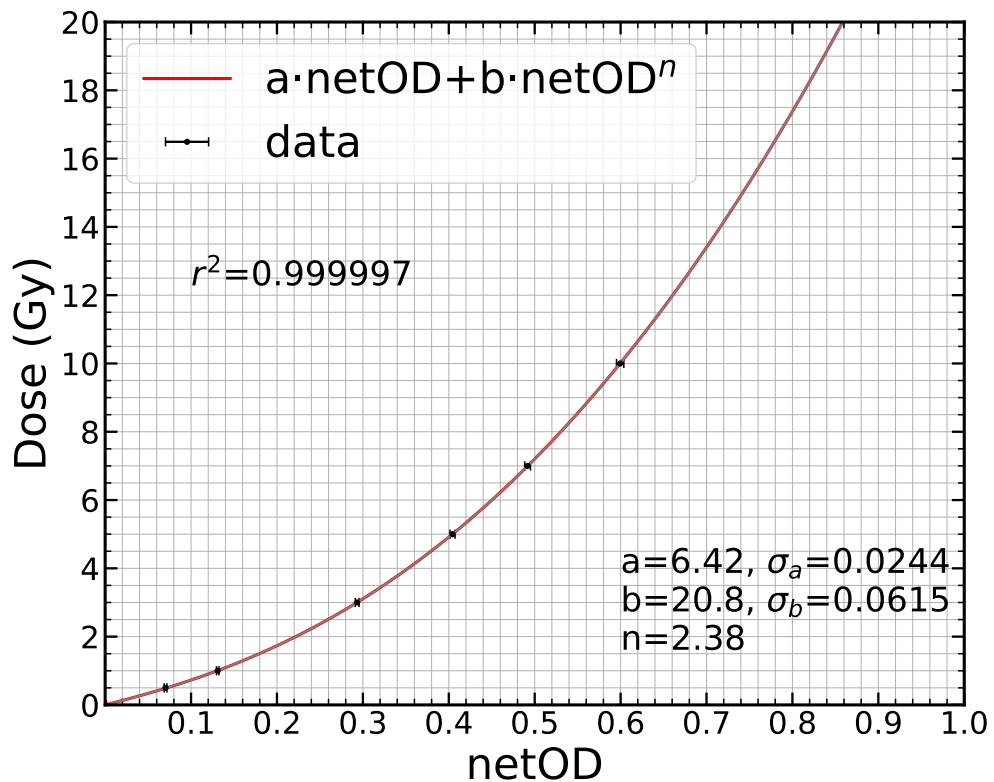


Figure 15: Calibration curve used for the EBT3 film dosimetry

plicity. Often, the complex mathematics needed in many analytical applications can be avoided entirely by simulation. Thus, Monte Carlo methods provide extremely powerful ways to address realistic problems that are not amenable to solution by analytic techniques. Today, with the widespread availability of powerful and inexpensive computers, Monte Carlo methods are widely used in almost every discipline that requires quantitative analysis.

In a Monte Carlo neutral-particle transport simulation, the geometry of the system is first specified, typically by combinatorial geometry, although other approaches can be used. Then by sampling from many distributions a complete simulation of a particle's track as it migrates through phase space can be obtained. Source sampling is required to pick the initial starting location, direction, and energy of a particle. Then sampling is used to pick a flight distance before a collision, followed by sampling to determine the type of collision. If the particle is not absorbed, more sampling is done to determine the type, direction, and energy of secondary particles. Each subsequent leg of the simulated track continues as

for the first leg. The particle is tracked until it is absorbed or leaves the problem boundary. As a particle moves along its trajectory, various tallies are updated so that, after many histories, some desired property of the radiation field can be estimated. To reduce computational effort, transport simulations often change the physical sampling distributions to bias a particle's track to increase the chance of it scoring [27].

2.4.1 FLUKA software description

FLUKA is a general purpose tool for calculations of particle transport and interactions with matter, that it is used for wide range of applications from proton and electron accelerator shielding to target design, dosimetry, detector design, cosmic rays, neutrino physics, radiotherapy etc. In FLUKA the use of microscopic models is common assuring consistency among all the reaction steps and/or reaction types. Conservation laws are enforced and results are checked against experimental data at single interaction level. Normally final predictions are obtained with a minimal set of free parameters fixed for all energy/target/projectile combinations. That is why results in complex cases, as well as properties and scaling laws, arise from the underlying physical models, also predictivity is provided where no experimental data is directly available.

FLUKA can simulate with high accuracy the interaction and propagation in matter of about 60 different particles, including photons and electrons from 100 eV-1 keV to thousands of TeV, neutrinos, muons of any energy, hadrons of energies up to 20 TeV (up to 10 PeV by linking FLUKA with the DPMJET code) and all the corresponding antiparticles, neutrons down to thermal energies and heavy ions. It can also transport polarised photons (e.g., synchrotron radiation) and optical photons. Time evolution and tracking of emitted radiation from unstable residual nuclei can be performed online.

FLUKA can work on very complex geometries, using an improved version of the well-known Combinatorial Geometry (CG) package. The FLUKA CG has been designed to track correctly also charged particles (even in the presence of magnetic or electric fields). For most applications, no programming is required from the user. However, a number of user interface routines (in Fortran 77) are available with special requirements. Also its double capability to be used in a biased mode as well as a fully analogue code [28].

2.4.2 Modeling of experiment with mouse phantom in FLUKA

In this section the general modeling procedure in FLUKA is described. To perform actual computation, FLUKA uses an input file (with extension .inp). This file describes the parameters for the program. So, the user need to correctly describe his problem under consideration in the input file, for that an ordinary text editor program can be used, but it is more convenient to use a graphic interface called Flair. In Flair we could define geometry of the experiment in a more convenient way and configure the contents of the input file. The definition of the geometry will depend on the specific application it is being investigated, this will simplify or complicate the simulation. Normally it is needed to define materials (compositions and densities of elements and mixtures) and geometrical shapes.

Later the source of radiation needs to be design taking into account energy spectrum, energy or angular spreading, position, etc. Next the physics model that rules over the simulation is selected, there are a set of default physics models. Although they are default they can be edit to get a better tune for our specific experiment.

Then estimators can be defined which can score Fluence, Kerma and other physical or dosimetric characteristics. These are obtained using various Monte Carlo techniques and algorithms behind these estimators are coded in FLUKA us-

ing Fortran language and accessible through the so-called cards.

The fluence scoring option used is based on a track-length (path-length), or on a collision estimator, they are called USRTRACK (or USRBIN) and USRCOLL respectively. For our case we use the USRBIN detector which provide the estimation of volume-averaged fluence for any type of particle or family of particles in any selected region, according to the equation [27]:

$$\bar{\Phi}_V \equiv \frac{1}{V} \int_V dV \int_{4\pi} \Phi(r, \Omega) d\Omega \simeq \frac{\sum_i^N W_i s_i}{NV} = \frac{S}{NV} \quad (34)$$

Where $\bar{\Phi}_V$ is the average fluence in the volume V , N is the total number of primaries in simulation, S is the weighted sum of path lengths tallied in that volume, W_i is the particle's weight applied and s_i is the particle track length in volume.

So, according to the formula, the volume normalisation is needed to obtain the fluence as track-length density. In our case USRBIN card calculates volumes itself. In case of USRTRACK the volume value needs to be input by the user, if none is given, the volume is assumed to be 1 cm^3 and the result will be respectively the total track-length in that region.

For our purposes we need to calculate doses inside the phantom and for that we defined USRBIN. But to score the dose depositions inside phantom, in the process of simulation photons need to produce electrons and there are not a huge amount of such events, so we would need a copious time to simulate this behavior well with low uncertainty. As an alternative we calculate Kerma, which under Charged Particle Equilibrium is equal to dose as we previously discussed in section 1.4.1, formula (22).

As for the calculation of Kerma, it is important to note that to obtain it, the weighting W_i needs to be changed to $E \cdot \left[\frac{\mu_{\text{en}}(E)}{\rho} \right]_{\text{med}}$, where E is the photon en-

ergy traveling path s_i in the volume and $\left[\frac{\mu_{\text{en}}(E)}{\rho} \right]_{\text{med}}$ is the mass energy-absorption coefficient corresponding to the specific material (med) of volume region. This technique allows us to estimate dose deposition in geometry more efficiently.

2.5 Experiment and modeling workflow

In this section we will describe the general workflow carried out, to perform the experiment, and modeling in order to clarify the procedure followed.

As explained in section 2.2 the phantom was prepared using that procedure. Later we obtained the films which were stored in recommended conditions, we proceeded to define the dimensions that we needed, in our case we used rectangles of 4 x 2.5 cm approximately. Then the process of marking and cutting was the same as the one explained in section 2.3.2. In our case, for clearance, we decided to use a simple notation for the films. We had four different setups (A, B, C, D) and 11 films for each so the notation on every film was placed on the right upper corner with the number first and then from which setup it was from as shown in figure 16.

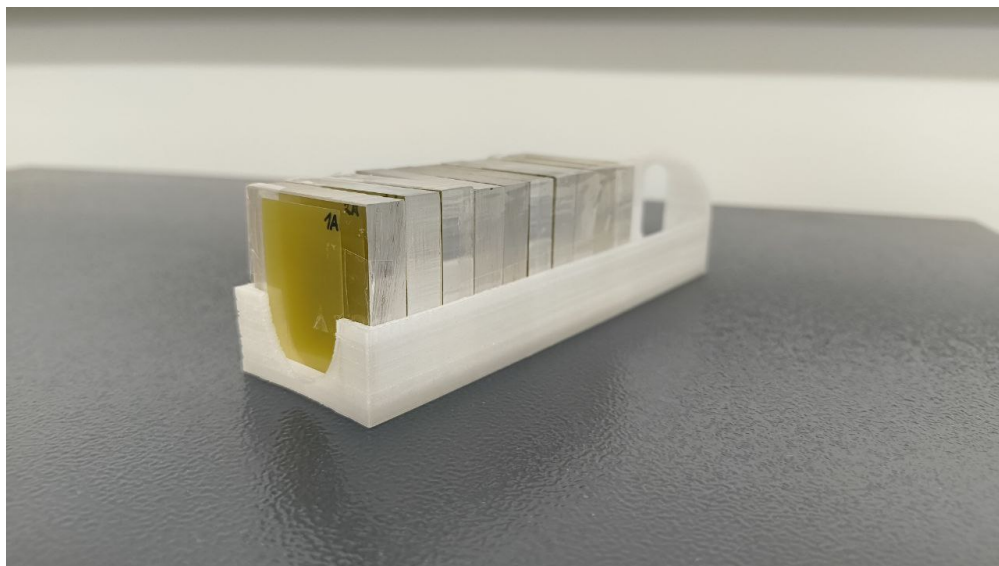


Figure 16: Phantom ready for the first irradiation.

After that we proceeded to use scotch tape for attaching the films to the slabs. Then, the produced phantom was taken to the SARRP facility (information

in section 2.1). On the SARRP facility, the work began with the warming of the machine, then the calibration of the detector for tomography, followed by the placing of the phantom (taking care of the laser alignment) as shown in figure 17.

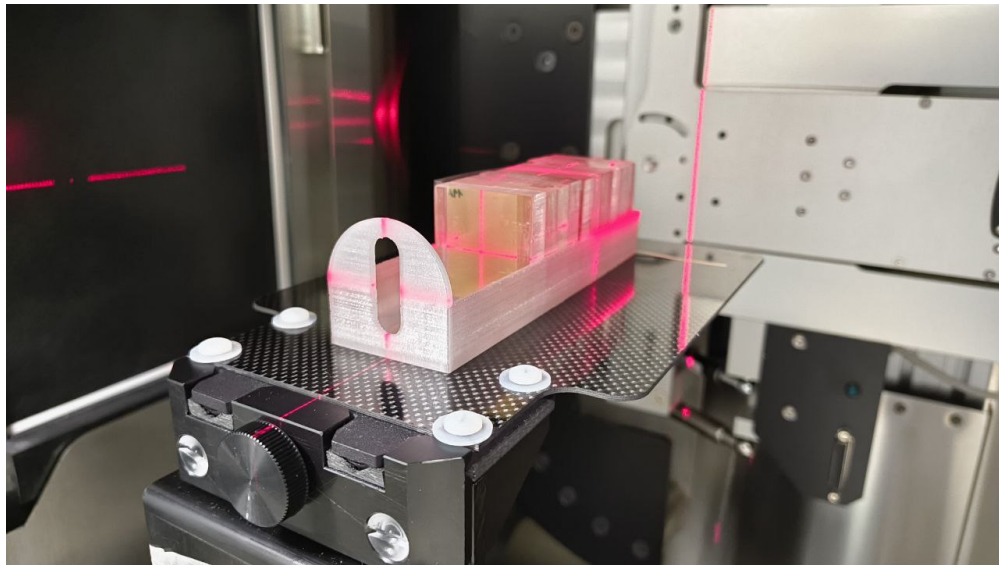


Figure 17: Mouse phantom placed for the irradiation in SARRP.

After that, we proceeded to do the tomography (with beam parameters of 70 kV, 1 mA, a fine focal spot and exposure time of 67 seconds). After the latter process we initialized MuriPlan treatment planning system and after loading the file of the tomography we reconstructed the geometry of the phantom. Sometimes the reconstructed geometry has some regions that do not belong to the real geometry (artifacts coming from scattered X-rays), so we get rid of them. Then we defined the isocenter on the center of the first film as shown in figure 18.

We defined the beam directions, assigned the desired dose, in our case 10 Gy, region type (we can choose the material for the geometry to be only water, or a combination of other materials) for the calculation of the dose distribution. Using MuriPlan program we defined small regions of interest (ROI) on films, so the program could calculate the dose on those ROI, this process is illustrated in figure 19.

We chose the dose engine (SC) to calculate dose and finally the program can start computing the doses. From the calculations made by MuriPlan we get Mean

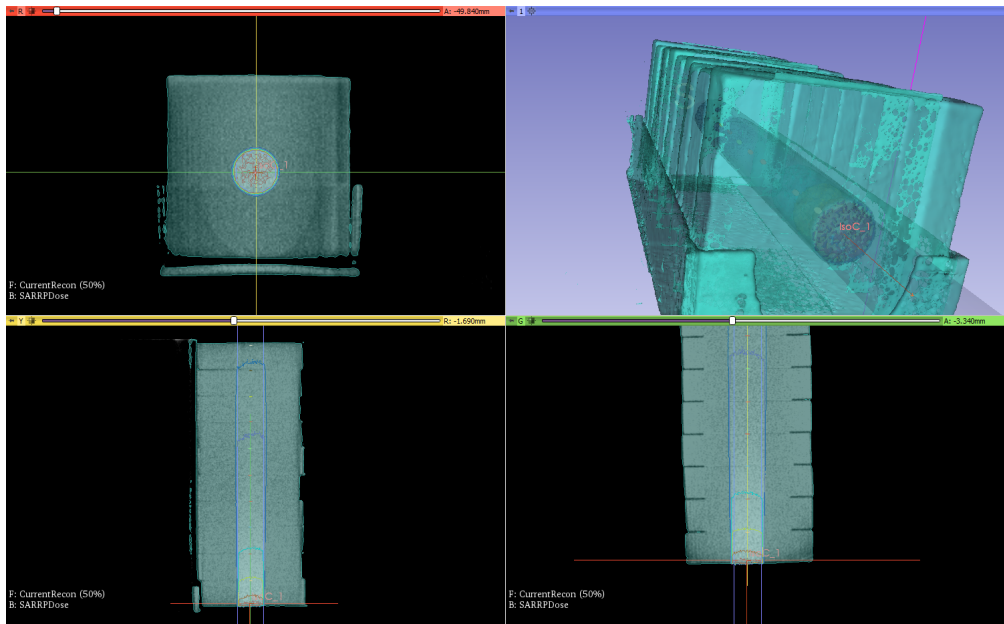


Figure 18: MuriPlan process of placement of isocenter.

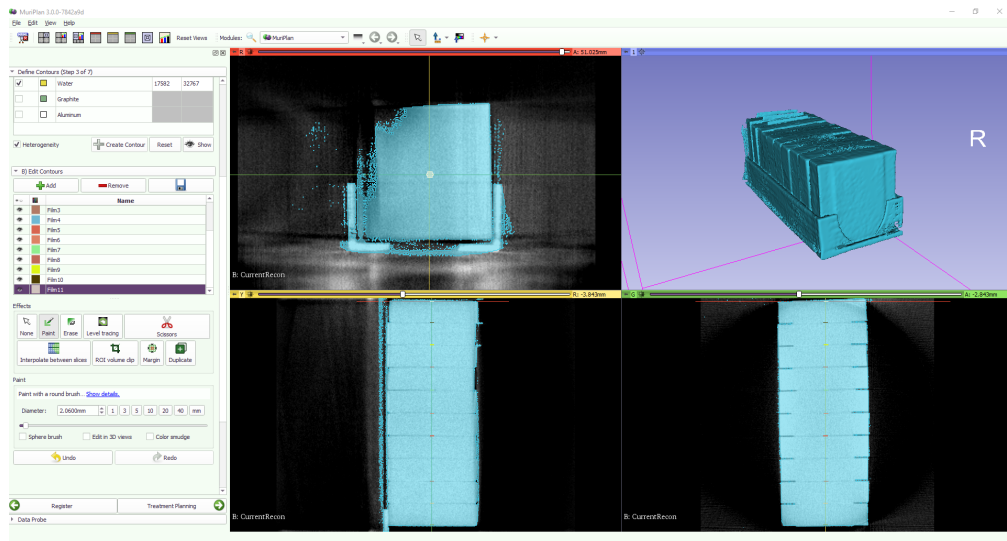


Figure 19: Definition of the ROI on MuriPlan.

Dose, Maximum Dose and Minimal Dose, which are then used in the analysis of the results and comparison with Film dosimetry and MC modeling.

In total, as explained above, we made 4 irradiations each one with different setup. We named them as A, B, C and D, to differentiate each set of films from the other, table 3 summarizes the parameters of each setup. In case of setups A and C the beam qualities are similar, the same happens for the case of setup B and D. This information is shown in table 4.

Table 3: Table of setups used in the experiments on the SARRP facility

Setups	A	B	C	D
Voltage (kV)	220	130	220	130
Current (mA)	13	13	13	13
Time of exposure (s)	171	173	192	510
Filter (mm)	Cu 0.15	Cu 0.15	Cu 0.15	Cu 0.15
Collimator Diameter (mm)	1	1	10	10

Table 4: Table of beam qualities used in the experiments on the SARRP facility

Beam quality №	1	2
Voltage (kV)	130	220
Filter (mm Cu)	0.15	0.15
Mean energy (keV)	60.67	78.11
First HVL Al/Cu (mm)	6.09/0.28	9.30/0.64
Second HVL Al/Cu (mm)	8.50/0.56	12.20/1.47
Homogeneity Coefficient Al/ Cu	0.71/0.50	0.76/0.43
Effective energy Al/Cu (keV)	46.40/49.23	60.31/66.63

After 24 hours from the irradiation, the films were scanned by the Epson Perfection V750 Pro, to obtain the data of the depth dose distribution along the phantom.

Now we describe the specifications in the Monte Carlo simulation carried on using FLUKA. To define geometry we used the GEOBEGIN card, in which we defined the isolation parallelepiped to restrict our experiment to a closed space. Then we defined the phantom parts, and then inside the phantom we defined the films using planes, of the correct sizes. Also we defined vacuum, where particle do not interact with anything at all. After we assigned the materials for each region, in the case of the phantom we used the water-equivalent material called PMMA with composition and density mentioned above and also for the EBT3 films.

To define estimators you need to include a different card for each one you need. We created an USRBDX card to confirm that the energy spectrum obtained by the simulation agrees with the one initially provided using SpekPy code [29].

We also included USRBIN cards for dose, fluence and Kerma scoring.

The Physics model selected was EM-CASCA (Pure electromagnetic cascade), also we define the threshold energy to 1 keV using the EMFCUT, for production and transport, so particles with energies above 1 keV are the only ones which are created and transported.

In our work, we developed a custom source algorithm using a FLUKA subroutine, initially named `source_newgen.f` and later modified to `XrayTube.f`. This subroutine, written in Fortran, allows the definition of particle positions and directions in a simulated X-ray tube setup. We also take into account the diameter of the source, depending on the collimator size in experimental setup.

Figure 20 provides a schematic representation of the radiation cone and the particle sampling process algorithm. On the right-hand side, a side view of the conical radiation field is shown. Particles are emitted within an angular spread, with the Z-axis being the forward direction.

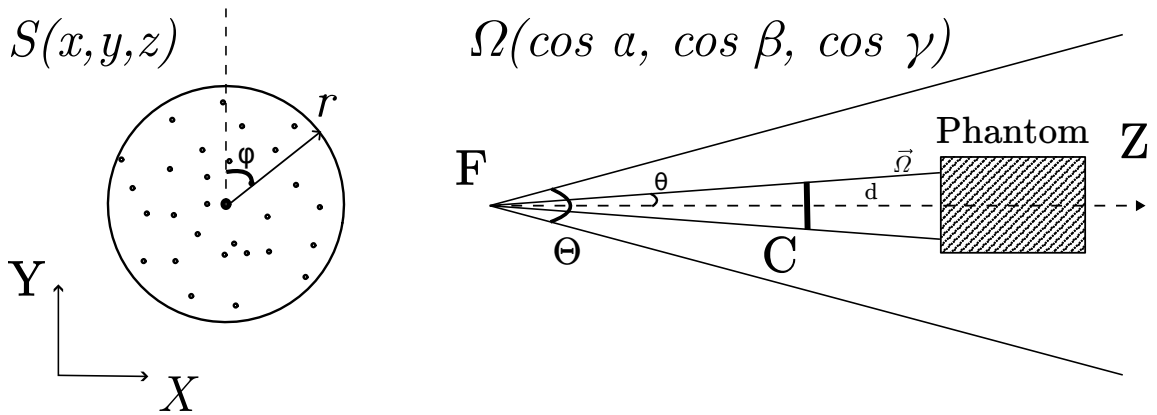


Figure 20: Schematic representation of the algorithm used for source definition.

The source is modeled as a circular cross-section of a radiation cone. Particles are emitted in the forward direction, along the Z-axis, at a distance (FC) of 30 cm from the focal point (F). To describe the position of each particle, we opted to use polar coordinates for simplicity, despite FLUKA's default Cartesian system.

The transformation from polar to Cartesian coordinates is given by:

$$\begin{cases} x = r \cos \varphi, \\ y = r \sin \varphi, \\ z = d, \quad \text{where } d = 30 \text{ cm is the fixed distance.} \end{cases}$$

For the angle φ , we sampled using a uniform probability density function (PDF) within the range $[0, 2\pi]$. Similarly, for the radial distance r , we used a uniform PDF, but to ensure proper sampling, each particle is assigned a weight that corrects bias to sample positions within circle randomly.

To describe the direction of emitted particles, we used spherical coordinates. The directional cosines are calculated as:

$$\begin{cases} \cos \alpha = \sin \theta \cos \varphi, \\ \cos \beta = \sin \theta \sin \varphi, \\ \cos \gamma = \cos \theta. \end{cases}$$

The angle θ is sampled using the geometric relationship:

$$\theta = \arctan \frac{r}{FC}, \quad (35)$$

where r is the radial distance, and FC is the distance from focal spot to the source position.

After defining source positions and directions we sampled energies of the photons correctly using data from the SpekPy [29]. For this purpose two spectra files were precalculated using the SARRP X-ray tube parameters in the code, stored and used in the source routine. In the end, all the source parameters were defined and the subroutine was compiled in FLUKA. After computation of the prepared input files the data was obtained and used to generate the corresponding graphs.

3 Results and discussion

As results from the experiment we got several plots, in order to understand them, in this section, we analyze them.

In Figures 21 and 22, the results for setups A and C are shown, comparing the same beam qualities (220 kV) with different collimator sizes: 1 mm — narrow beam and 10 mm — broad beam.

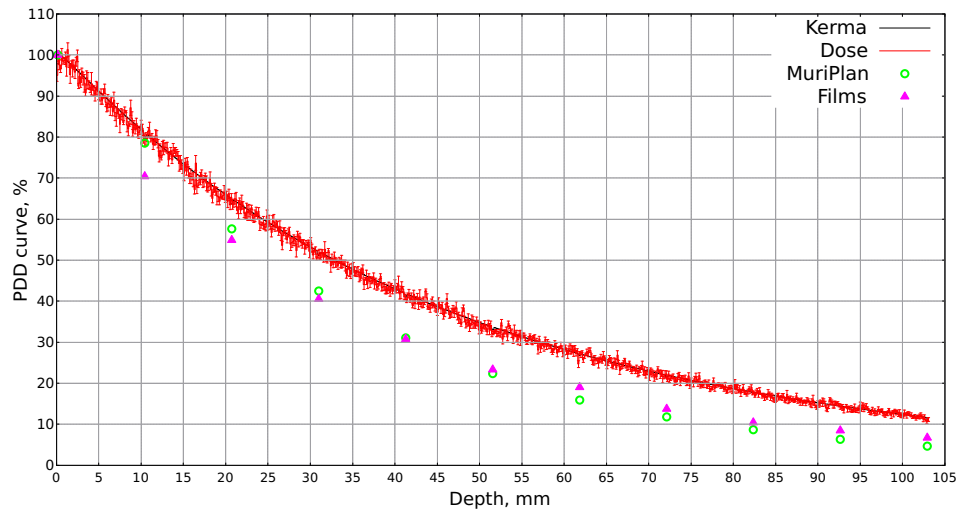


Figure 21: Percentage depth dose (PDD) curve for the setup A (220 kV + 1 mm) with data from experiments and modeling.

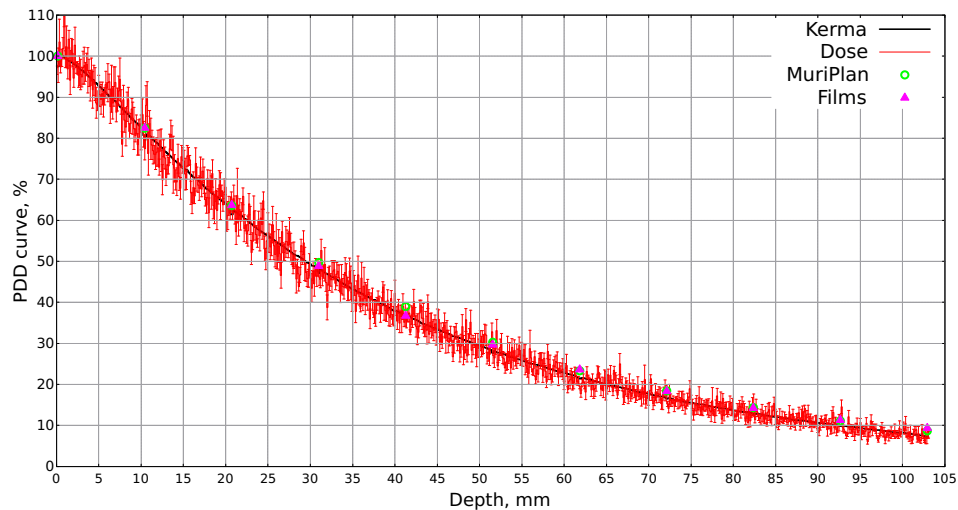


Figure 22: Percentage depth dose (PDD) curve for the setup C (220 kV + 10 mm) with data from experiments and modeling.

While the dose results suggest that more statistical data is needed, it's im-

important to note that, under CPE conditions, Kerma is equivalent to dose as discussed before, making Kerma a more reliable metric for analysis. All of the data were normalized to the value of the first film on the surface. In setup A, the discrepancies increase along the phantom, reaching a maximum of 10% around 62 mm. For setup C, the maximum discrepancy is 3% at 42 mm. The notable difference in discrepancies can be attributed to variations in setups: beam quality, collimator size. In setup A, the Monte Carlo simulation may exhibit deviations due to a potential source definition issue, whereas in setup C, the simulation performs more accurately.

In the following figures 23 and 24, the results from setups B and D are shown, comparing the same beam qualities (130 kV) with different collimator sizes (1 mm and 10 mm).

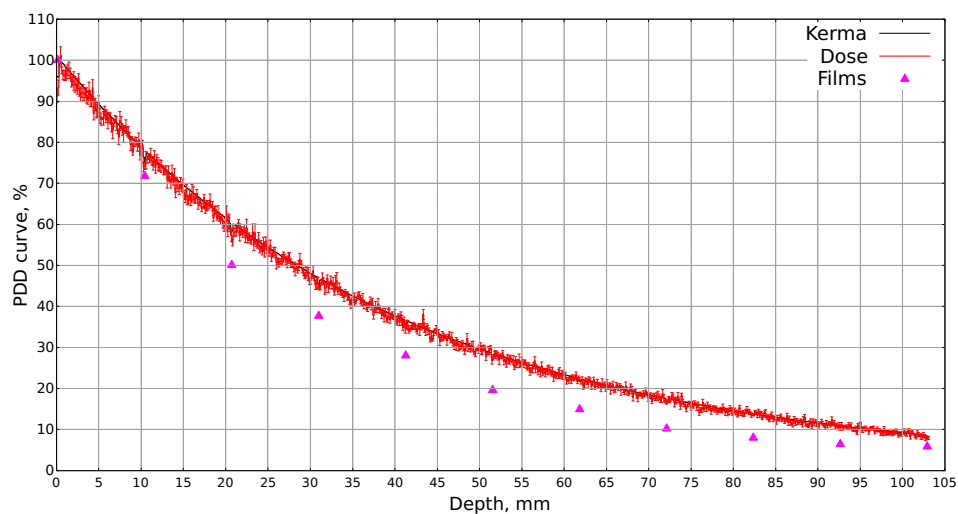


Figure 23: Percentage depth dose (PDD) curve for the setup B (130 kV + 1 mm) with data from experiments and modeling.

In these plots the MuriPlan predictions are not shown because the program is incapable of calculate the dose with this beam quality (130 kV). Here we can appreciate that the biggest discrepancy for setup B is around 9% and it arises around 52 mm. For setup D the biggest discrepancy is around 1% and arises around 42 mm. This case reinforces what was mentioned above about the problem presented by the source definition in modeling in the case of the smallest collimator.

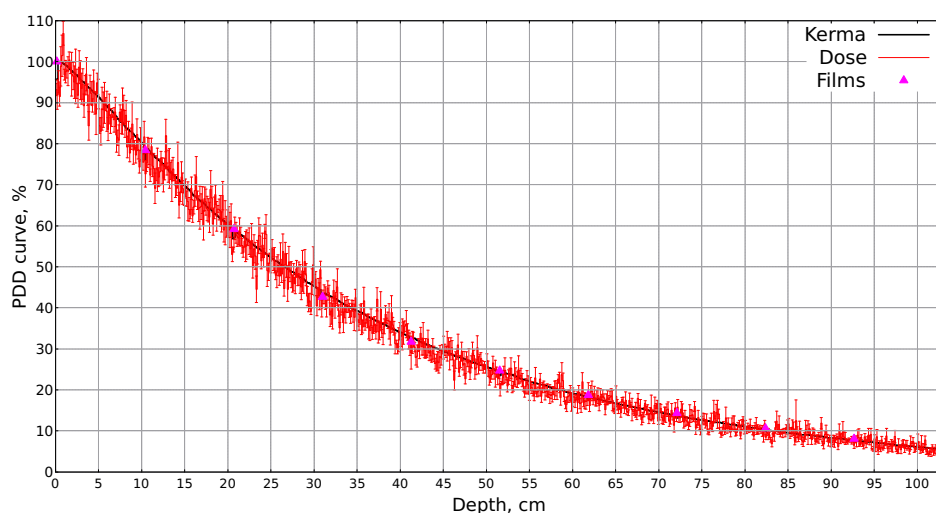


Figure 24: Percentage depth dose (PDD) curve for the setup D (130 kV + 10 mm) with data from experiments and modeling.

In Figures 25 and 26, we observe the narrow beam with a small spreading from the central axis: on the entrance is about 1 mm and in the final film is about 2 mm. The symmetry of the beam relative to the y-axis is evident, indicating a well-modeled behaviour of the collimator. Additionally, we can identify the distance from the central axis at which the dose drops significantly, in this case around 1 mm, as well as the main region of the dose administration. In both instances, these findings align with our expectations, demonstrating that the central zone effectively delivers the intended dose. This analysis further validates the adequacy of the collimator size, which corresponds to the required measurement of 1 mm.

In Figures 27 and 28, we can see the flatness of the radiation beam produced by FLUKA, meanwhile in the case of data the flatness is restricted to an area from -5 mm to 3 mm. This behavior can be attributed to the known heel effect, which is a phenomenon that is produced due to the positioning of the anode, which reduces the fluence of particles from the anode side. We can also distinguish the penumbra zone, which is the zone where the dose decreases gradually because it is away from the main zone of incidence. This zone changes with the film due to the spreading of the beam, each time it goes through a film, the maximum spreading can be seen,

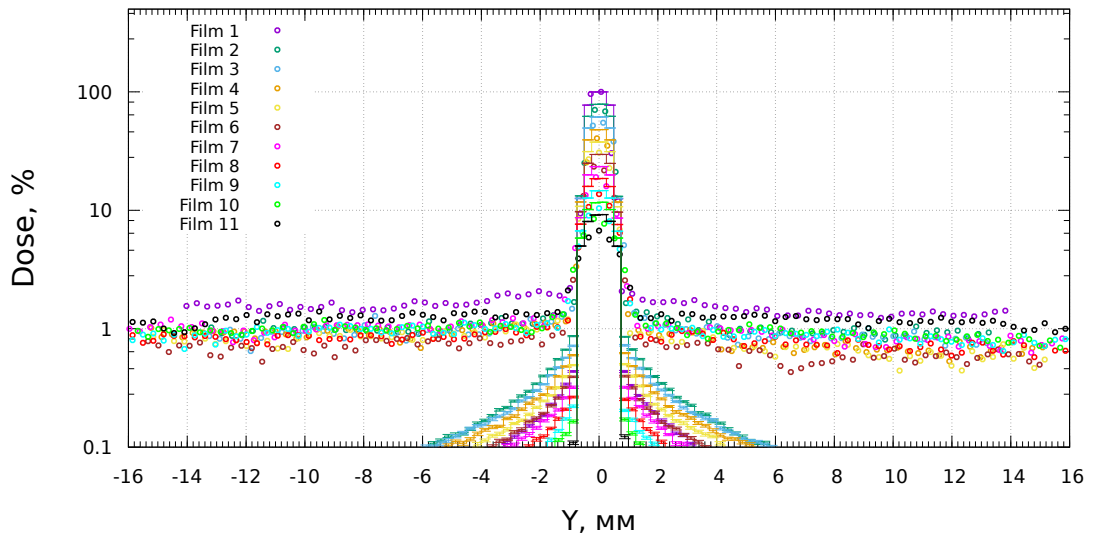


Figure 25: Profiles of the beam along Y axis (vertical) for measurements (circles) with films and modeling (lines) for the setup A (220 kV + 1 mm).

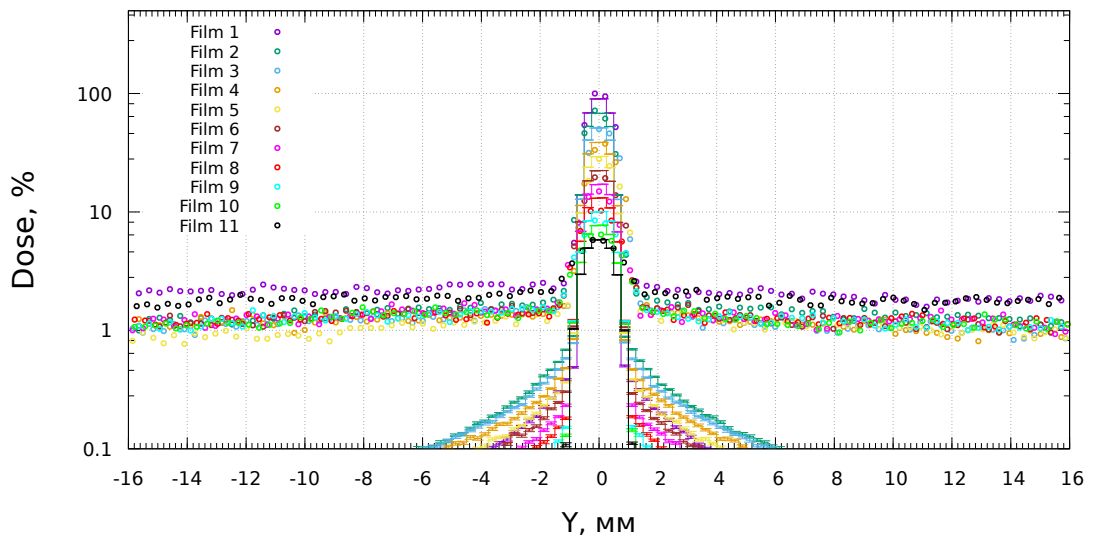


Figure 26: Profiles of the beam along Y axis (vertical) for measurements (circles) with films and modeling (lines) for the setup B (130 kV + 1 mm).

as expected. In the last film, the flatness is about 12 mm, so it is a 2 mm spread for both cases, respect the initial incidence zone. In both cases, these observations confirm our expectations and illustrate that the central region successfully delivers the desired dose. This analysis further supports the appropriateness of the collimator size, which is aligned with the necessary measurement of 10 mm.

In Figures 29 and 30, the distribution of Kerma on the Z-Y plane is presented, corresponding to the setups A and B respectively with narrow beam.

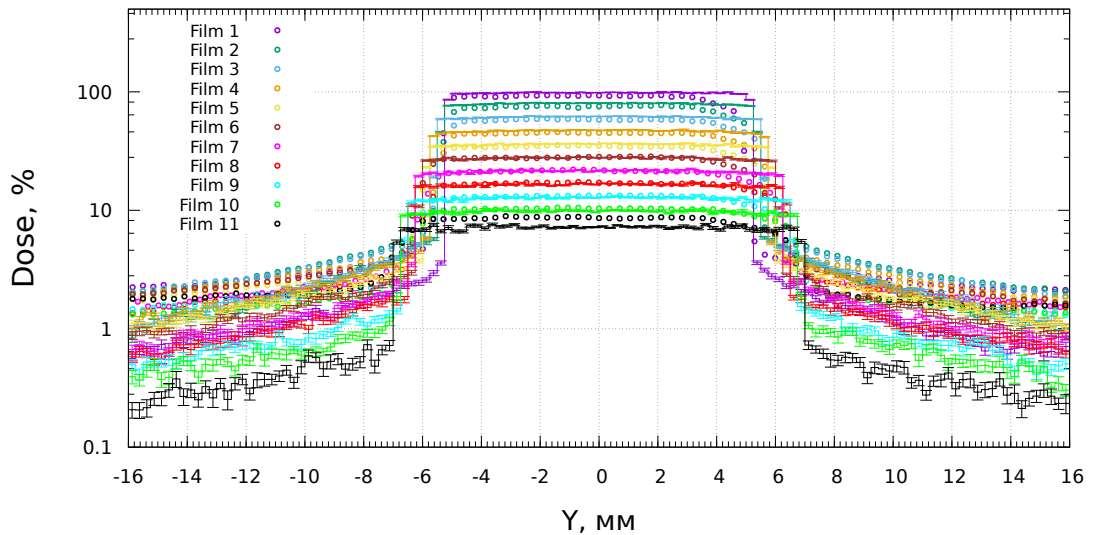


Figure 27: Profiles of the beam along Y axis (vertical) for measurements (circles) with films and modeling (lines) for the setup C (220 kV + 10 mm).

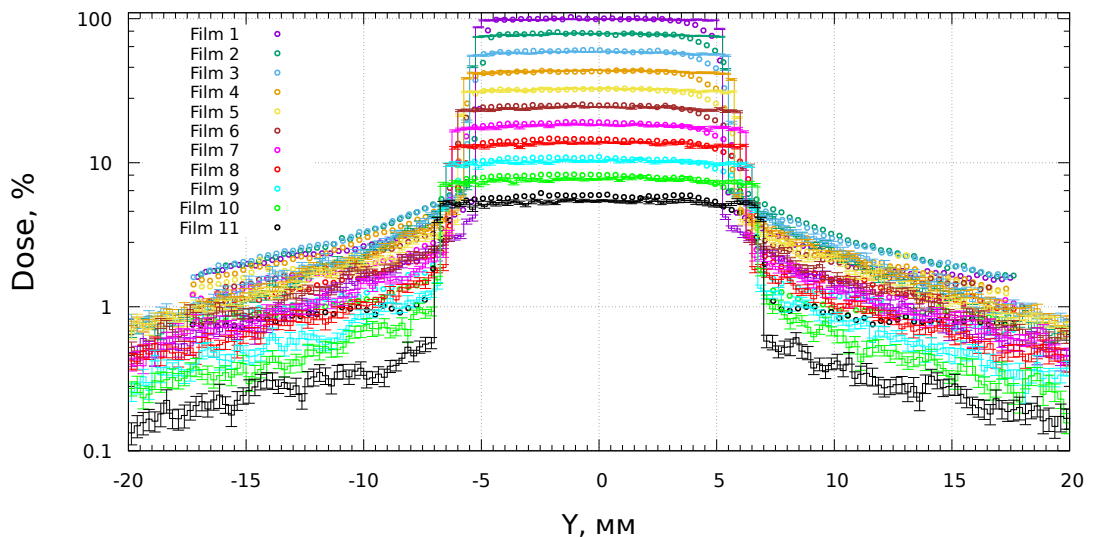


Figure 28: Profiles of the beam along Y axis (vertical) for measurements (circles) with films and modeling (lines) for the setup D (130 kV + 10 mm).

As expected, moving away from the central axis to the sides of the beam reveals a significant decrease in Kerma values due to low scattering of particles in lateral directions. Initially, Kerma reaches its maximum near the surface where the radiation beam is stronger. However, as the beam penetrates deeper into the phantom, the Kerma gradually decreases, due to the attenuation of particles. In setup A, this attenuation occurs more gradually compared to setup B, which is explained by the harder beam spectrum in setup A. The higher energy photons in

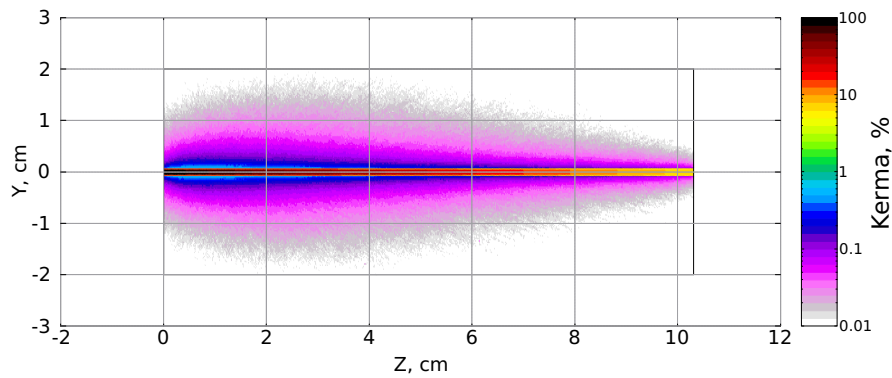


Figure 29: 2D projection of the spatial distribution of the Kerma on the Z-Y plane for the setup A (220 kV + 1 mm).

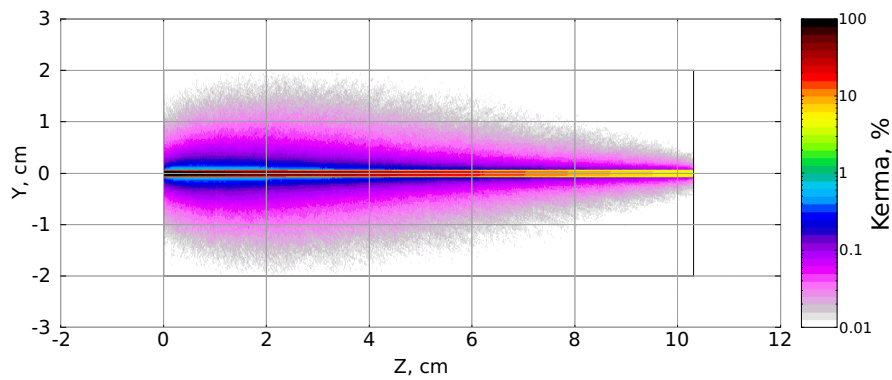


Figure 30: 2D projection of the spatial distribution of the Kerma on the Z-Y plane for the setup B (130 kV + 1 mm).

setup A have greater penetration power, resulting in a slower decrease in Kerma. In contrast, setup B, with softer beam spectrum, shows faster attenuation. In both of these cases the effect of the beam, in the surroundings at 1.5 cm from the central axis has almost disappear (about 10000 times lower in dose), so lateral sizes of the phantom are shielding completely the beam.

In Figures 31 and 32, the distribution of Kerma on the Z-Y plane is presented, corresponding to the setups C and D respectively with broad beam.

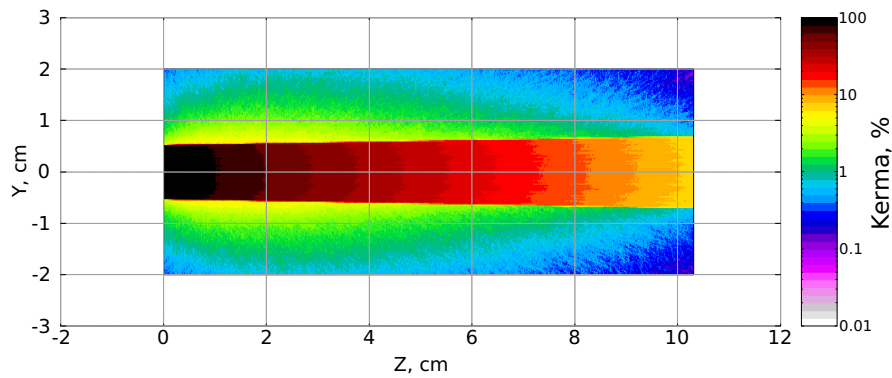


Figure 31: 2D projection of the spatial distribution of the Kerma on the Z-Y plane for the setup C (220 kV + 10 mm).

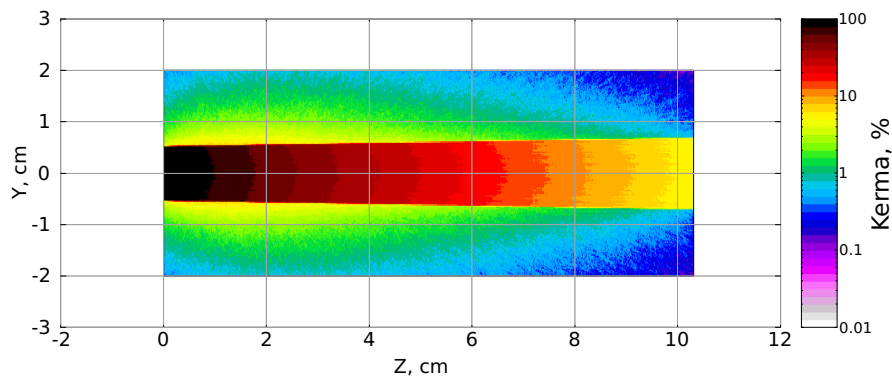


Figure 32: 2D projection of the spatial distribution of the Kerma on the Z-Y plane for the setup D (130 kV + 10 mm).

As one moves laterally from the central beam axis, there is a noticeable decrease in Kerma, indicating the scattering of radiation. Initially, near the beam's center-line, the Kerma is at its peak due to the highest photon flux, but as the radiation penetrates through the phantom, this value steadily drops.

The rate of attenuation differs between setup C and setup D. For setup C, the attenuation is slower, which can be attributed to the higher energy of the radiation beam produced by the increased voltage (harder beam spectrum). This allows deeper penetration before the radiation is fully absorbed. In contrast, setup D, with

a lower applied voltage, results in a quicker drop in Kerma, signifying that lower energy photons (softer beam spectrum) are more readily absorbed within the initial layers of the phantom. In both of these cases the effect of the beam in the surroundings of the beam at 2 cm from the central axis still affecting with a Kerma above 1 %, meaning that lateral sizes of the phantom are not shielding completely the beam in these cases with broad beam.

Figure 33 presents a comparison of the modeling results of Kerma depth distribution for each setup, summarizing all the curves obtained from simulation.

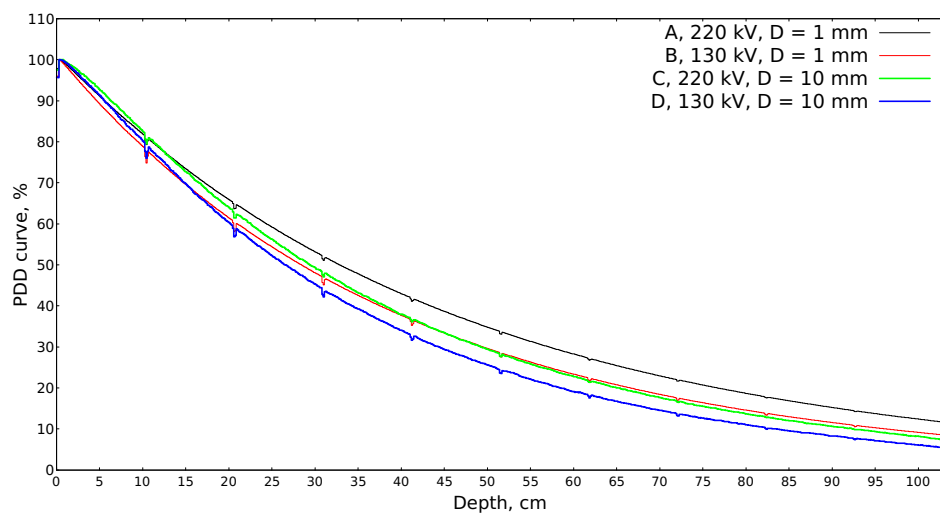


Figure 33: Comparison of the curves for all the setups from FLUKA modeling.

The discontinuities visible in the curves reflect the places where films are situated in the modeling geometry, they are a bit different in density and composition to the PMMA plates. We cannot analyze these curves in depth, because, as it was shown on the Figures 21 and 23, the modeling curves do not align with the measurement results.

Conclusion

During this summer session, I became familiar with several essential tools for my development as a scientist, including GnuPlot, L^AT_EX, and ImageJ. These tools are not only relevant to the work presented in this report, but are broadly applicable across various fields of research. In relation to the topic of this report, I engaged with extensive bibliography and acquired a foundational understanding of the key concepts.

The use of the SpekPy tool proved invaluable, as it is frequently required in dosimetry work. The fundamental knowledge of dosimetry principles gained during this session will be crucial for the development of my bachelor's thesis. Additionally, familiarizing myself with the capabilities of the SARRP machine was particularly beneficial, as this was my first experience working with such equipment, providing me with valuable hands-on experimental experience.

Working with radiochromic films introduced me to a different type of dosimeter, expanding my knowledge beyond the devices I have previously used. The work with the phantom was also entirely new to me, and this initial experience lays the groundwork for future applications of this technique. Lastly, learning to use the FLUKA software represents a significant step forward, and this report serves as a foundation for further development of my skills with the program.

Experimental and simulation results show that both beam energy and collimator size have a significant impact on the dose distribution within the phantom. Higher energy beams (220 kV) produced higher dose penetration, while smaller collimators (1 mm) allowed a more concentrated dose delivery, with less energy dissipation. The plots obtained from the film dosimetry measurements, together with Monte Carlo simulations using FLUKA, not only successfully replicated the

experiment, but also confirmed the validity of the MuriPlan predictions. Although, there is a still discrepancy of modeling results and measurements for narrow beam setups considered, which may be improved by introducing more accurate beam spreading.

Furthermore, the experimental results confirm that the calibration of EBT3 films remains accurate and reliable to date. The consistency between film dosimetry results and simulations (broad beam case) reinforces the reliability of the methods used, demonstrating that the SARRP system is capable of providing accurate radiation planning and delivery in small animal models. This work provides valuable data to improve dosimetric practices in preclinical research, leading to better results in radiobiology studies.

References

1. *Poludniowski G., Omar A., Andreo P.* Calculating X-ray Tube Spectra [Text]. — CRC Press, 2012.
2. *Elford J. H., Robert C. J.* The Physics of Radiology. — Springfield : Charles C. Thomas, 1983.
3. Filters. — URL: <https://radiopaedia.org/articles/filters>.
4. *Dance D., Agency I. A. E.* Diagnostic Radiology Physics: A Handbook for Teachers and Students. — International Atomic Energy Agency, 2014. — (STI/PUB). — URL: <https://books.google.ru/books?id=9iiKmwEACAAJ>.
5. X-ray Data Booklet. — URL: <https://xdb.lbl.gov/xdb-new.pdf>.
6. Small Animal Radiation Research Platform SARRP Comprehensive Guide [Text]. — Precision, 07/2018.
7. COMPREHENSIVE GUIDE — Xstrahl MuriPlan, Software Version 3.0.0 [Text]. — Xstrahl, 2024.
8. House Mouse. — URL: <https://www.britannica.com/animal/house-mouse>.
9. IAEA TRS-398. Absorbed Dose Determination in External Beam Radiotherapy: An International Code of Practice for Dosimetry based on Standards of Absorbed Dose to Water [Text] / P. Andreo [et al.]. — IAEA, 2006.
10. *Maegan A. Gargett Adam R. Briggs J. T. B.* Water equivalence of a solid phantom material for radiation dosimetry applications [Text] // Elsevier. — 2020.
11. *M.M.M. SARCAR K. MALLIKARJUNA RAO K. L. N.* Computer Aided Design and Manufacturing [Text]. — PHI Learning Pvt. Ltd., 2008.
12. Autodesk Inventor: 3D modeling software for designers and engineers. — URL: <https://www.autodesk.com/products/inventor/overview?term=1-YEAR&tab=subscription>.
13. What Is FDM 3D Printing? – Simply Explained. — URL: <https://all3dp.com/2/fused-deposition-modeling-fdm-3d-printing-simply-explained/>.
14. *Wochnik A., Swakoń J., Olko P.* WATER EQUIVALENCE OF VARIOUS 3D PRINTED MATERIALS FOR PROTON THERAPY — MONTE CARLO SIMULATION, TREATMENT PLANNING MODELLING AND VALIDATION BY MEASUREMENTS [Text] // Acta Physica Polonica. — 2019.

15. PETG site. — URL: https://en.wikipedia.org/wiki/Polyethylene_terephthalate.
16. Film-Dosimetry: an overview. — URL: <https://oncologymedicalphysics.com/film-dosimeters/>.
17. Dosimetric characterization of GafChromic EBT3 films in Volumetric Modulated Arc Therapy (VMAT) radiotherapy treatments. — URL: <https://core.ac.uk/download/pdf/129672848.pdf>.
18. Evaluation of a LED-based flatbed document scanner for radiochromic film dosimetry in transmission mode [Text] / J. M. Lárraga-Gutiérrez [et al.] // *Phys Med*. — 2018. — P. 86–91.
19. *González-López A., Vera-Sánchez J., Ruiz-Morales C.* The incidence of the different sources of noise on the uncertainty in radiochromic film dosimetry using single channel and multi-channel methods [Text] // *Phys Med Biol*. — 2017. — P. 25–36.
20. Grid patterns, spatial inter-scan variations and scanning reading repeatability in radiochromic film dosimetry [Text] / I. Méndez [et al.] // *Phys Med*. — 2016. — P. 72–81.
21. How flatbed scanners upset accurate film dosimetry [Text] / L. van Battum [et al.] // *Phys Med Biol*. — 2015. — P. 25–49.
22. *Lewis D., Chan M. F.* Correcting lateral response artifacts from flatbed scanners for radiochromic film dosimetry [Text] // *Med Phys*. — 2015. — P. 16–29.
23. *Lewis D., Devic S.* Correcting scan-to-scan response variability for a radiochromic film-based reference dosimetry system [Text] // *Med Phys*. — 2015. — P. 692–701.
24. The artefacts of radiochromic film dosimetry with flatbed scanners and their causation by light scattering from radiation-induced polymers [Text] / A. A. Schoenfeld [et al.] // *Phys Med Biol*. — 2014. — P. 75–97.
25. *Alnawaf H., Yu P. K., Butson M.* Comparison of Epson scanner quality for radiochromic film evaluation [Text] // *J Appl Clin Med Phys*. — 2012.
26. Precise radiochromic film dosimetry using a flat-bed document scanner [Text] / S. Devic [et al.] // *Medical Physics*. — 2005.
27. *Dunn J. W. L., Shultis K.* *Exploring Monte Carlo Methods* [Text]. — Barcelona : Elsevier, 2012.
28. FLUKA website. — URL: <https://fluka.cern/>.

29. Technical Note: SpekPy v2.0—a software toolkit for modeling x-ray tube spectra / G. Poludniowski [et al.] // Medical Physics. — 2021. — Vol. 48, no. 7. — P. 3630–3637. — URL: <https://aapm.onlinelibrary.wiley.com/doi/abs/10.1002/mp.14945>.